

# Improving Understanding of Atmospheric River Water Vapor Transport using a Three-Dimensional Straightened Composite Analysis

Guangzhi Xu<sup>1</sup>, Lin Wang<sup>2</sup>, Ping Chang<sup>3</sup>, Xiahui Ma<sup>4</sup>, and Shuyu Wang<sup>5</sup>

<sup>1</sup>Beijing Normal University

<sup>2</sup>Institute of Atmospheric Physics, Chinese Academy of Sciences

<sup>3</sup>TAMU

<sup>4</sup>Ocean University of China

<sup>5</sup>Key Laboratory of Physical Oceanography and Frontiers Science Center for Deep Ocean Multispheres and Earth System

November 21, 2022

## Abstract

The irregular shapes of atmospheric rivers (ARs) and the scarcity of sounding data have hampered easy AR composite analyses and understandings about AR's moisture transport mechanism. In this work we develop a method to composite AR-related variables from a reanalysis dataset. By averaging a large number of samples, the three dimensional structure and some evolutionary features of a typical North Pacific AR are revealed. An AR is typically located along and in front of the surface cold front of an extratropical cyclone. A meso-scale secondary circulation is observed in the cross-sections of the AR corridor, where both geostrophic and ageostrophic winds make indispensable contributions to the strong moisture transport. Geostrophic moisture advection across the cold front within the Equatorward half of the AR is created by the baroclinicity of the system, and serves as the primary moisture source of the AR-resided atmosphere. Moisture fluxes from the warm sector of the cyclone are primarily due to ageostrophic winds within the boundary layer, and are more important within the poleward half the AR, particularly during the genesis stage. The faster movement speed of the AR compared with low level winds enables the ARs to collect downwind moisture. While within the Equatorward half moisture transport is mostly attributed to geostrophic advection carried along by the propagating AR-cyclone couple. Driven by the intensifying geostrophic winds, ARs tend to reach peak moisture transport intensity about two days after genesis. Then reduced moisture and influxes from lateral boundaries prevent further moisture flux intensification.

1 **Improving Understanding of Atmospheric River Water**  
2 **Vapor Transport using a Three-Dimensional**  
3 **Straightened Composite Analysis**

4 **Guangzhi XU<sup>1</sup>, Lin WANG<sup>2</sup>, Ping CHANG<sup>3,4</sup>, Xiaohui MA<sup>5</sup>, Shuyu WANG<sup>5</sup>**

5 <sup>1</sup>College of Global Change and Earth System Science, Beijing Normal University, Beijing, China. ORCID:  
6 0000-0001-5877-5608

7 <sup>2</sup>Center for Monsoon System Research, Institute of Atmospheric Physics, Chinese Academy of Sciences,  
8 Beijing, China

9 <sup>3</sup>Department of Oceanography and Department of Atmospheric Sciences, Texas A&M University, College  
10 Station, Texas, USA

11 <sup>4</sup>The International Laboratory for High-Resolution Earth System Prediction, Texas A&M University,  
12 College Station, Texas, USA

13 <sup>5</sup>Key Laboratory of Physical Oceanography and Frontiers Science Center for Deep Ocean Multispheres  
14 and Earth System, Ocean University of China / Qingdao Pilot National Laboratory for Marine Science  
15 and Technology, Qingdao, China

16 **Key Points:**

- 17 • Develops a new method to composite atmospheric rivers with irregular shapes and  
18 orientations.
- 19 • Reveals the meso-scale secondary circulation across the atmospheric river and high-  
20 lights the relationship with frontogenesis processes.
- 21 • Depicts the 3D structure of moisture transports within an atmospheric river and  
22 the different geostrophic and ageostrophic contributions.

---

Corresponding author: Guangzhi XU, [xugzhi1987@gmail.com](mailto:xugzhi1987@gmail.com)

## Abstract

The irregular shapes of atmospheric rivers (ARs) and the scarcity of sounding data have hampered easy AR composite analyses and understandings about AR's moisture transport mechanism. In this work we develop a method to composite AR-related variables from a reanalysis dataset. By averaging a large number of samples, the three dimensional structure and some evolutionary features of a typical North Pacific AR are revealed. An AR is typically located along and in front of the surface cold front of an extratropical cyclone. A meso-scale secondary circulation is observed in the cross-sections of the AR corridor, where both geostrophic and ageostrophic winds make indispensable contributions to the strong moisture transport. Geostrophic moisture advection across the cold front within the Equatorward half of the AR is created by the baroclinicity of the system, and serves as the primary moisture source of the AR-resided atmosphere. Moisture fluxes from the warm sector of the cyclone are primarily due to ageostrophic winds within the boundary layer, and are more important within the poleward half the AR, particularly during the genesis stage. The faster movement speed of the AR compared with low level winds enables the ARs to collect downwind moisture. While within the Equatorward half moisture transport is mostly attributed to geostrophic advection carried along by the propagating AR-cyclone couple. Driven by the intensifying geostrophic winds, ARs tend to reach peak moisture transport intensity about two days after genesis. Then reduced moisture and influxes from lateral boundaries prevent further moisture flux intensification.

## 1 Introduction

Researches on the salient lower tropospheric moisture fluxes, now commonly known as “atmospheric rivers” (ARs), can be dated back to the 1970s (K. A. Browning & Pardee, 1973). It has also been related to concepts including the warm conveyor belt (WCB), tropical moisture exports and low level jets (LLJs) (e.g. Bao et al. (2006); Knippertz et al. (2013); Zhu and Newell (1998); Gimeno et al. (2014)). As the research matures and ambiguities are being clarified, the community has arrived at the term “atmospheric rivers”, with a formal definition of “a long, narrow and transient corridor of strong horizontal water vapor transport that is typically associated with a LLJ stream ahead of the cold front of an extratropical cyclone.” (Ralph et al., 2018). This definition summarizes the most prominent features of ARs, and also ties the phenomenon to its key physical driving factors.

A number of earlier works lay the foundations for the understandings of the AR-related physical processes. Newell and Zhu (1994); Zhu and Newell (1994, 1998) suggested a close relationship between ARs and cold fronts, by observing the spatial coincidence of such filamentary structures and extratropical storm tracks. The baroclinicity and humidity gradients associated with frontal systems give rise to a net poleward heat and moisture transport (Zhu & Newell, 1998). A key contributor to the enhanced moisture transport is the pre-frontal LLJ found in the warm sector of an extratropical cyclone (Ralph et al. (2004) and references therein). To help fully capture the narrow transverse structures of ARs, direct measurements were collected from dropsondes and rawinsondes (Ralph et al., 2004, 2005, 2017). These sounding measurements observationally quantify the amount of water vapor transported by ARs, and also help establish the relationship between ARs and meso-scale frontal structures. A detailed analyses on the development of ARs and frontogenesis processes are given in a case study by Cordeira et al. (2013), using the frontogenesis function to indicate the location and strength of the secondary ageostrophic circulation across the AR corridor. The strengthening effect of frontogenesis on ARs has also been documented by Neiman et al. (2013). On the other hand, Z. Zhang et al. (2019) performed a statistical analysis on the co-occurrences of ARs and extratropical cyclones. Their results showed that 82% of Eastern Pacific ARs are associated with an extratrop-

74 ical cyclone, and there exists mutual intensification mechanisms between these two phe-  
75 nomena.

76 However, existing studies on the structures and dynamics of ARs have left some  
77 knowledge gaps. Firstly, it is noticed that analyses on the structures or evolutions of ARs  
78 have been largely relying on case studies (e.g. Neiman et al. (2013); Bao et al. (2006);  
79 Ralph et al. (2005, 2017); Cordeira et al. (2013)). Few studies have analyzed the gen-  
80 eral dynamical changes following the AR life cycle by taking a large population of ARs  
81 into consideration. Based on the averages of Pacific and Atlantic ARs during 2005-2016,  
82 Xu et al. (2020a) documented an early intensification and a subsequent weakening of AR  
83 IVT during the life cycle, but no physical explanation was given to the possible causes  
84 of such a change. Zhou et al. (2018) documented some kinematic characteristics of North  
85 Pacific ARs following their life cycle, including their traveled distances, propagation speeds  
86 and pathways, yet structural or dynamical analyses are lacking. Secondly, most previ-  
87 ous works have focused on the along-AR moisture fluxes/winds in their cross-sectional  
88 analyses (e.g. Newell and Zhu (1994); Ralph et al. (2004); Cordeira et al. (2013); Ralph  
89 et al. (2017)), and few has analyzed the roles played by the cross-AR fluxes/winds. It  
90 has been argued that ARs collect considerable amount of moisture from the surround-  
91 ing atmosphere (Bao et al., 2006; Cordeira et al., 2013; Dacre et al., 2019), however, it  
92 is not clear how the moisture from the lateral boundaries of the AR get aggregated and  
93 contributes to the strong AR IVT. The distribution of cross-sectional winds associated  
94 with the frontal structure is likely the key to answering this question.

95 The scarcity of large sample AR composite analyses in literature is largely due to  
96 their complex shapes. Unlike tropical cyclones, storms or ocean eddies whose circular  
97 symmetry allows for relatively straightforward composite analysis (e.g. Knaff et al. (2014);  
98 Jourdain et al. (2014); X. Zhang et al. (2019); Frenger et al. (2013)), the irregular shapes  
99 of ARs deny such a convenience. As a work-around, and so motivated by the physical  
100 relationship with extratropical cyclones, some studies adopted a cyclone-centric perspec-  
101 tive, and created composites by aligning up the extratropical cyclones that are found to  
102 have an accompanying AR (Zhu & Newell, 1994; Dacre et al., 2015; Eiras-Barca et al.,  
103 2018; Dacre et al., 2019; Z. Zhang et al., 2019). This gives the broad configuration of the  
104 AR-cyclone couple. However, the AR and its accompanying cyclone do not form a rigid  
105 relationship, but with considerably varying distances (Z. Zhang et al., 2019). Therefore,  
106 some of the more delicate meso-scale structures in the cross-sections of the ARs may be  
107 lost. On the other hand, sounding observations can provide an accurate cross-sectional  
108 view of an AR, but suffer from limitations of data availability and representativeness.  
109 Existing literature based on sounding data are spatially confined to the near coastal re-  
110 gions of the Northeastern Pacific, and can not support a full life cycle analysis on long-  
111 lived ARs originated from the western Pacific. This may imply a big limitation of this  
112 approach, considering that many of the North America landfalling ARs are originated  
113 from the Kuroshio Extension region (Liu et al., 2021). The relative roles played by large-  
114 scale geostrophic processes and the ageostrophic, secondary frontal circulation can not  
115 be revealed using sounding data alone (Ralph et al., 2004). Furthermore, satellite im-  
116 ages lack the ability to resolve the vertical structure of the AR, and surface wind speed  
117 measurements are often contaminated by heavy precipitation (Ralph et al., 2004).

118 In view of such limitations, we develop a method to process and “straighten” the  
119 AR-related variables in a reanalysis dataset to a composite-ready form. The resultant  
120 composites can be used to depict the general three dimensional structure of an AR. We  
121 aim to use such information to explain how North Pacific ARs collect moisture from the  
122 surrounding atmosphere, their relationship with extratropical cyclones and cold fronts,  
123 and how the AR associated IVT is affected by dynamical and thermodynamical changes  
124 following their life cycle.

125 The important role played by ARs in poleward moisture transport has been widely  
126 acknowledged (e.g. Zhu and Newell (1998); Ralph et al. (2004); Xu et al. (2020a); Ralph

127 et al. (2020)). However, the exact manner in which they achieve the transport has raised  
 128 some debates in literature. There are broadly two competing views regarding the mois-  
 129 ture transports by ARs, one suggests a direct transport of moisture from the low lati-  
 130 tudes along the corridor of the AR all the way to the mid-latitude target regions (e.g.  
 131 Newell and Zhu (1994); Wick et al. (2013); Neiman et al. (2013)), and the other empha-  
 132 sizes the local recycling of moisture and the replenishment from tropical and extratrop-  
 133 ical sources (e.g. Bao et al. (2006); Dacre et al. (2015, 2019)). In particular, Dacre et  
 134 al. (2019) proposed a “feeder-airstream” mechanism to explain the moisture sources for  
 135 an AR-cyclone system. However, their composites only cover a 1500 *km* radius around  
 136 the cyclone center, and may not provide a complete picture of the AR. Therefore, we  
 137 also aim to give an AR-centric depiction of the moisture transport pattern, and to of-  
 138 fer an answer to the question of how ARs transport moisture in the Earth- and AR-relative  
 139 frames of reference.

140 This work is organized follows. Section 2 introduces the dataset and the compositing  
 141 methods. Section 3 gives analyses on the straightened AR composites, by first show-  
 142 ing the typical AR-cyclone relationship in a plane-view perspective in Section 3.1, fol-  
 143 lowed by the cross-sectional views in Section 3.2. The geostrophic and ageostrophic winds  
 144 have different levels of importance in the along-front and cross-front directions. Their  
 145 contributions to the thermodynamic and dynamic processes of AR evolutions are dis-  
 146 cussed in Section 3.3-3.4. The moisture transport pattern by a typical AR is explored  
 147 in Section 3.5, in the Earth- and AR-relative frames of reference, respectively. The key  
 148 findings are summarized in Section 4, with some discussions on the implications and lim-  
 149 itations of the work.

## 150 2 Methodology and data

### 151 2.1 Reanalysis data

152 Three dimensional air temperature ( $T$ ), geopotential height ( $Z$ ), specific humid-  
 153 ity ( $q$ ) and winds ( $u$ ,  $v$  and  $w$ ) during 2004-Jan to 2010-Dec are obtained from ECMWF’s  
 154 ERA-INTERIM (ERA-I) reanalyses product (Dee et al., 2011). All data have a horizon-  
 155 tal resolution of  $0.75^\circ$  and a temporal resolution of 6 hours. IVT is computed from lay-  
 156 ered  $u$ ,  $v$  and  $q$  by vertically integrating across the atmosphere column. The choice of  
 157 the reanalysis product has been shown to be an insignificant factor to AR detection re-  
 158 sults (Ralph et al., 2018). The  $0.75^\circ$  resolution of ERA-I data is close to the average 80 *km*  
 159 dropsonde spacing of Ralph et al. (2017) and is sufficient to resolve cross-sectional struc-  
 160 tures of ARs.

### 161 2.2 AR detection and tracking

162 ARs at individual time points are detected using the magnitude-independent de-  
 163 tection algorithm documented in Xu et al. (2020b). By relaxing the requirement on the  
 164 IVT magnitude and instead performing the filtering based on the spatio-temporal scales  
 165 of the ARs, this detection method is less sensitive to parameter choices, and can more  
 166 reliably retain ARs at the genesis or dissipating stages when their IVT strengths are gen-  
 167 erally weaker. The same AR entity appearing in consecutive time slices are tracked us-  
 168 ing the “simple-path” tracking method as introduced in Xu et al. (2020b).

### 169 2.3 AR straightening method for scalar fields

170 To create composites of ARs they are first straightened along their axes. The AR  
 171 axis is a summary of the AR’s geometry, and is defined as the array of grid cells inside  
 172 the AR that has the largest along-path IVT integral (see Xu et al. (2020b)). By defi-  
 173 nition, the axis is directed in that it follows the general directions of moisture fluxes within  
 174 the AR. This enables the identification of the first and last axis points regardless of the

175 shape, curvature and orientation of the AR. The axis is smoothed by a 10-point mov-  
 176 ing average to remove small-scale curvatures.

177 The straightening method is inspired by similar techniques used to straighten im-  
 178 ages of human chromosomes (e.g. Jahani and Kamaledin Setarehdan (2012); Arora et  
 179 al. (2017)). Like ARs, chromosomes may appear as straight, bent and at various orien-  
 180 tations in their microscope scans. To straighten an AR, slices of a given scalar variable  
 181 (e.g.  $IVT^1$ ) are taken from perpendicular profiles sampled along the AR axis. These equal-  
 182 length profiles are re-stacked to form a “resample matrix”, from which the straightened  
 183 image is constructed using bi-linear interpolation. More technical details are given in the  
 184 Appendix, and Fig. 1 gives an example of the straightening process applied on the  $IVT$   
 185 field of a Northeastern Pacific AR at 2004-Jan-04, 18:00 UTC. The AR boundary is drawn  
 186 as black contour, and the axis as dotted curve from the starting point  $S$  to the end point  
 187  $E$  (Fig. 1a). It can be seen in Fig. 1b that the axis and profiles form a “fish-bone-like”  
 188 structure. The straightened image in Fig. 1c is oriented such that the starting point  $S$   
 189 is on the left hand side and the end point  $E$  on the right. Based on the thermal wind  
 190 relationship, this implies that the bottom side, where the AR width axis is labeled neg-  
 191 ative, corresponds to the warm side, and the top is the cold side. This orientation is also  
 192 consistent with the natural coordinate system often used in frontal system studies (e.g.  
 193 Hoskins and Bretherton (1972); Keyser et al. (1988)). The straightened image is then  
 194 normalized along the x-axis to give the length-normalized straightened image in Fig. 1d,  
 195 which now has a fixed dimension and is therefore composite-ready. The binary mask de-  
 196 lineating the AR region is also straightened using the same process, and re-discretized  
 197 to binary using a cut-off value of 0.5.

198 It can be seen in Fig. 1b that when an AR displays considerable curvature, the pro-  
 199 file lines may cross over each other where the AR bends inward, and may create some  
 200 artifacts in the straightened image. Therefore, we also experimented constructing the  
 201 profile lines using two curvilinear grids stitched together at the AR axis. An example  
 202 is given in Fig. S1 in the Supplementary. As a curvilinear grid is quasi-orthogonal, it is  
 203 immune to the crossing-profiles issue. After interpolation, this creates more natural look-  
 204 ing straightened images (Fig. S1c,d), but the broad structure is largely consistent, par-  
 205 ticularly in the interior of the AR where it is so narrow that virtually no crossing-over  
 206 happens. After averaging across a large sample, the difference between the two approaches  
 207 is negligible (two comparisons are given in Fig. S2 and S3). Therefore, the rest of the  
 208 work is based on results from the “fish-bone” straightening method alone.

## 209 2.4 AR straightening method for vector fields

210 The above straightening method only works for scalar fields as the directional in-  
 211 formation of a vector field is not preserved during the process. To faithfully straighten  
 212 a vector field, the azimuthal angle of each profile is first computed, then the original vec-  
 213 tor direction sampled at each point along the profile is rotated by that amount accord-  
 214 ingly, such that the rotated profile aligns with the y-axis in the straightened image. More  
 215 details on the computation of this rotation angle is given in the Appendix. A nearest-  
 216 neighbor interpolation is used to interpolate the vector directions onto the target grid,  
 217 to avoid artifact values across the 0/360 degree joint. Only vector directions are straight-  
 218 ened in this manner, the u- and v- components of the vectors, respectively correspond-  
 219 ing to the x- and y- dimensions in the straightened image, are recovered from the straight-  
 220 ened scalar magnitudes and directions.

221 Fig. 1c, d also show the straightened  $IVT$  field of the same AR case. It can be seen  
 222 that the process achieves a satisfactory retention of the regional circulation patterns. The

---

<sup>1</sup> in AR researches the term  $IVT$  is often used to refer to the scalar magnitude  $|IVT|$  and the vector field  $IVT$  interchangeably. We will use bold font to emphasis a vector definition in later sections.

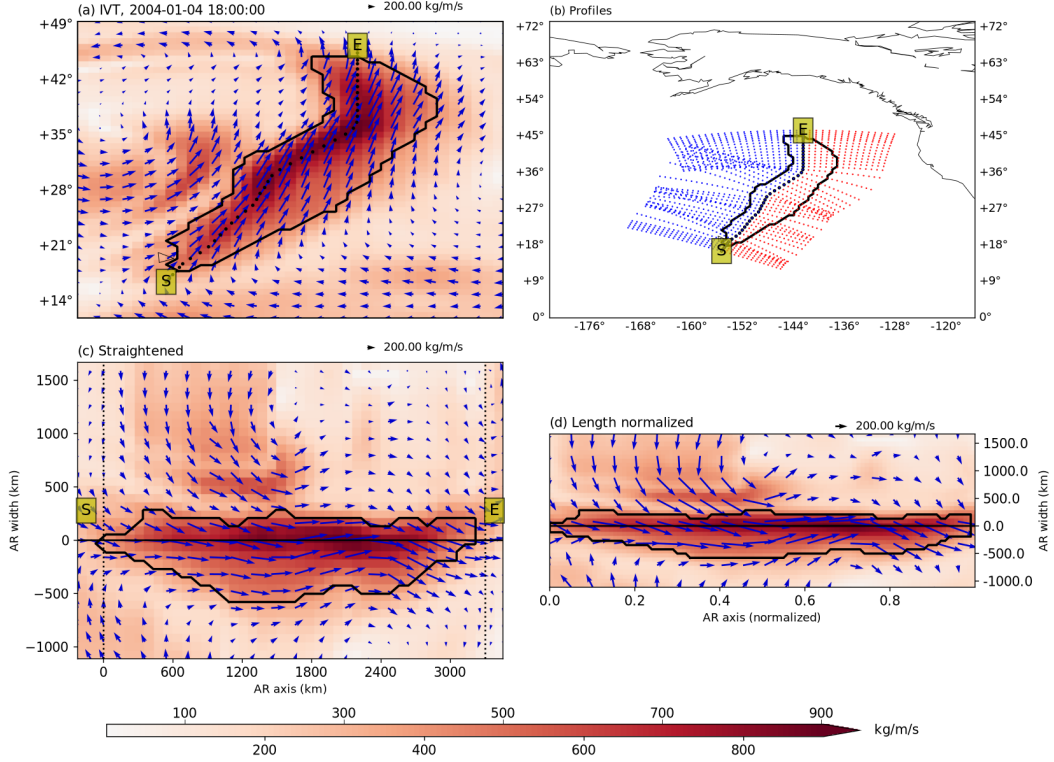


**Figure 1.** Illustration of the scalar and vector field straightening method. (a) IVT (in  $kg/(m\ s)$ ) distribution of an AR over the Northeastern Pacific at 2004-Jan-04 18 UTC. Magnitudes of IVT are shown as colors, and flux vectors are superimposed on top. The boundary of the AR is drawn as black contour, and the axis is drawn as the dotted curve starting from the starting point  $S$  to the end point  $E$ . (b) axis and cross sectional profiles of the same AR. Profiles are drawn crossing each axis point perpendicular to the local line segments, with “warm side” profile points drawn in red and “cold side” points in blue. “Warm side” profile limb covers a longitude/latitude distance of  $10^\circ$  with 14 evenly spaced sample points, and “cold side” limb covers a distance of  $15^\circ$  with the same spacing. (c) straightened IVT of the AR. Perpendicular profiles as shown in (b) are re-stacked from the starting point  $S$  to the end point  $E$  along the x-axis, and scalar IVT is computed from the re-stacked coordinates using bi-linear interpolation. Vector directions are rotated according to the orientation of the profile line. The binary mask of the AR region is also interpolated and re-discretized to binary with a cut-off value of 0.5. (d) straightened IVT of the AR normalized to a fixed shape of  $36 \times 100$ , where 36 is the dimension of the AR width, and 100 the dimension of the AR length.

223 cyclonic (anti-cyclonic) cell on the cold (warm) side of the AR is well preserved after the  
 224 straightening, as well as the sharp clockwise turn observed at the southern tip of the AR.

### 225 3 Results

#### 226 3.1 Plane-view composites of ARs and the relationship with extratrop- 227 ical cyclones

228 North Pacific ARs during 2004-2010 are first detected and tracked. After filtering  
 229 by a  $120^{\circ}E-100^{\circ}W$  longitudinal range, about 25600 6-hourly AR occurrences ( $\sim 3657$   
 230 per year) are obtained. Some basic statistics about these ARs are given in Fig. S4. The  
 231 straightening methods described above are applied on ERA-I data to create composites  
 232 of various variables. Besides the example given in Fig. 1, four more cases, covering a length  
 233 span of  $\sim 3500 - 6500 km$ , are given in the supplementary Fig. S5-S8. It can be seen  
 234 that the straightening methods work reasonably well on ARs with a wide range of lengths.  
 235 There are some minor differences in the straightened composites between different length  
 236 categories (not shown), however, the basic structures within and around the ARs are con-  
 237 sistent. Therefore, for the sake of depicting the general structure of a typical North Pa-  
 238 cific AR, it is acceptable to average ARs across the entire length span. However, there  
 239 are cases when the sizes or locations of the ARs are important. In such situations, fur-  
 240 ther constraints, for instance, specifications on the locations of the starting and ending  
 241 points of the AR axis, are imposed to obtain a composite with more coherent samples.  
 242 Such constraints will be specified when explaining relevant analyses.

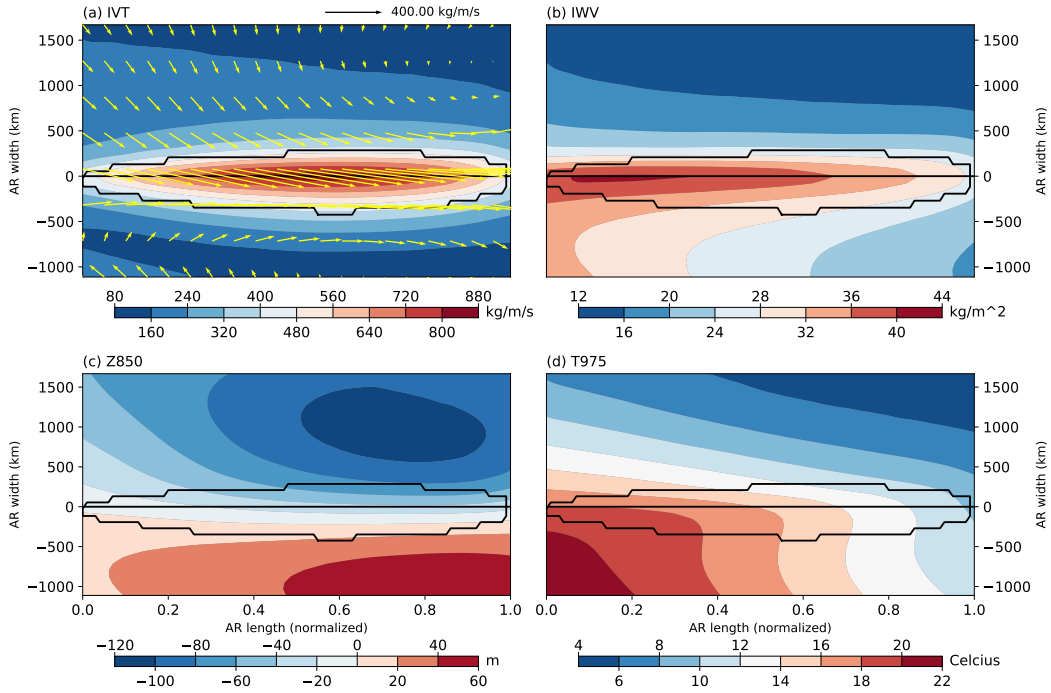


**Figure 2.** Composites of (a) IVT (magnitude shown as color shading, in  $kg/(m s)$ ), and vectors as arrows), (b) IWV (in  $kg/m^2$ ), (c) geopotential height anomalies at 850 hPa level (in m) and (d) air temperature at 975 hPa level (in Celsius). Composites are created by averaging the straightened fields of North Pacific ARs during the period of 2004-2010. Black contours delineate the averaged boundaries of ARs, and the thin black line the axis of the AR.

243 Fig. 2 displays the composites of some horizontal fields. It can be seen that the com-  
 244 posite of the straightened AR has a shuttle-like shape, with a slightly wider warm side  
 245 than the cold side, particularly in the middle section of the AR. This is also observed  
 246 in the case shown in Fig. 1. The straightened **IVT** field is cyclonic on the cold side and  
 247 anti-cyclonic on the warm side (Fig. 2a). The two circulations converge at the AR re-  
 248 gion, but with a component towards the warm side. This may explain the observed shape  
 249 asymmetry that the moisture is “pushed” towards the warm side, and is also consistent  
 250 with the integrated water vapor (IWV) distribution in that the maximum IWV centers  
 251 at the axis but skews towards the warm side (Fig. 2b). Unlike the IVT field that has pointed  
 252 ends, the IWV field is well connected with high IWV levels outside of the AR region on  
 253 the left side of the straightened image (Fig. 2b). Considering that most Northern Hemi-  
 254 sphere ARs have a southwest-northeast orientation, the left end corresponds to the tail  
 255 of the AR where the atmosphere in lower latitudes has higher vapor contents.

256 Consistent with the circulation pattern, the 850 *hPa* geopotential height anom-  
 257 alies ( $Z850'$ , with respect to the zonal average) feature a low (high) pressure center on  
 258 the cold (warm) side (Fig. 2c). This dipole pattern was also identified in Z. Zhang et al.  
 259 (2019), who suggested that the high pressure center is important for ARs that are not  
 260 associated with a cyclone. Boundary layer air temperature composite shows a warmer  
 261 “bottom-left” quadrant, a largely horizontal temperature gradient in the *x*- direction on  
 262 the warm side of the AR, and a sharper *y*- direction temperature gradient across the cen-  
 263 tral line (Fig. 2d). This justifies the warm and cold side definitions. The warmer quad-  
 264 rant having higher IWV distribution is also consistent with the Clausius-Clapeyron re-  
 265 lationship (e.g. Held and Soden (2006)).

266 These plane-view composites allude to a typical AR-cyclone relationship: an AR  
 267 tends to appear around the southeastern edge of a cyclone, aligning along and in front  
 268 of the cold front<sup>2</sup>. To help depict this AR-cyclone relationship in a geographic map pro-  
 269 jection, a subset of 300 ARs are randomly selected from those whose starting point falls  
 270 within the box of  $20\text{--}35^\circ N$ ,  $125\text{--}140^\circ E$ , and ending point the box of  $40\text{--}55^\circ N$ ,  $145\text{--}$   
 271  $160^\circ E$ . Composites of IVT, IWV,  $Z850'$  and T975 are shown in Fig. S9 in Supplemen-  
 272 tary. The relationship between the AR and the extratropical cyclone is consistent with  
 273 the above descriptions. Similar configurations are also observed in composites created  
 274 from ARs in other longitudinal bands within the North Pacific (not shown). Therefore,  
 275 this AR-cyclone relationship is a rather consistent feature, suggesting that the trailing  
 276 AR propagates with the accompanying cyclone. This explains the similarities between  
 277 the AR track and storm track (Zhu & Newell, 1998; Xu et al., 2020a), and that the for-  
 278 mer is slightly equatorward in comparison (Mundhenk et al., 2016).

279 It should be noted that the similar AR-cyclone configuration has been documented  
 280 by earlier studies from a cyclone-centric perspective (e.g. Dacre et al. (2015, 2019); Z. Zhang  
 281 et al. (2019)). However, the extent of an AR’s width is much smaller than the radius of  
 282 an extratropical cyclone, and some of the more delicate structures, for instance, the cross-  
 283 sectional profiles, may be obscured if the AR samples are not accurately aligned up. The  
 284 next section focuses on such vertical structures.

### 285 3.2 Vertical structures of ARs

286 By applying the same straightening and compositing methods on variables at var-  
 287 ious vertical levels, the three dimensional structure of a typical AR is reconstructed. The  
 288 straightened fields are further normalized along the width dimension, by aligning up the  
 289 AR axes, and interpolating the cold and warm sides separately to a normalized width  
 290 of 1.0 and  $-1.25$ , respectively. The 25% extra warm side width is determined from the

---

<sup>2</sup> based on this, we use “cross-front” and “along-front” interchangeably with “cross-axis” and “along-axis”.

291 averaged AR mask. Taking the widest cross-section within the middle 25 – 75% por-  
 292 tion of the AR length, the average AR width is about  $\sim 800\text{ km}$ , which is partitioned  
 293 into  $355\text{ km}$  ( $455\text{ km}$ ) on the cold (warm) side, based on the 1 : 1.25 ratio. Note that  
 294 the average  $800\text{ km}$  width is wider than the median width of  $500\text{ km}$  as shown in Fig.  
 295 S4. Aside from the difference between mean and median in a non-Gaussian distribution,  
 296 this is also because the latter is defined as the “effective width”, i.e. the ratio of area over  
 297 length. The narrower ends of the AR region make the effective width smaller than the  
 298 width measured at the widest cross-section.

299 Fig. 3a shows the cross-sectional composite of along-axis moisture fluxes at 50%  
 300 of the AR length. The moisture flux profile features an asymmetrical dome-like shape,  
 301 with a flatter base on the warm side. This is consistent with the AR shape asymmetry  
 302 mentioned previously, and also explains the raised (suppressed) 50, 75 and 90% IVT height  
 303 levels on the cold (warm) side. These IVT height levels are obtained by integrating the  
 304 along-axis moisture fluxes from the bottom level up. Therefore, at the core of the AR,  
 305 75% of the total IVT is found below  $\sim 650\text{ hPa}$ , and only about 10% above the level  
 306 of  $\sim 500\text{ hPa}$ . Compared with moisture fluxes, the specific humidity profile does not  
 307 have as clear lateral boundaries (Fig. 3b), but features a more gradual decline from the  
 308 center of the AR. However, humidity level also drops much faster on the cold side. The  
 309 asymmetrical humidity distribution and the tilt of the moisture fluxes towards the cold  
 310 side are consistent with sounding observations (Ralph et al., 2004, 2017).

311 The asymmetrical humidity distribution is related to the thermodynamical condi-  
 312 tions. Isotherms slope down towards the cold side, with a zone of strong baroclinic-  
 313 ity (horizontal temperature gradient  $\leq -1\text{K}/100\text{ km}$ , shown as grey shading in Fig. 3a)  
 314 on the cold side. The frontal line which is marked by the dash-dotted blue curve in Fig. 3,  
 315 represents the maximum (negative) temperature gradient at each level, and tilts away  
 316 from the AR center and towards the upper level low pressure center (Fig. 3c). On one  
 317 hand, baroclinicity of the system leads to low equivalent potential temperature (Fig. 3d)  
 318 and low humidity (Fig. 3b) on the cold side. (Due to a faster decreasing rate of temper-  
 319 ature with respect to humidity, the relative humidity level is actually higher on the cold  
 320 side (Fig. 3d)); On the other hand, tightened isotherms across the cold front induce en-  
 321 hanced vertical wind shear via the thermal wind relationship, creating an upper level jet  
 322 situated above the surface cold front (Fig. 3c). The along-front wind enhancement also  
 323 extends from the tropopause down to the boundary layer level, where a LLJ is observed  
 324 (Fig. 3c). It is also interesting to notice that the zero  $Z850'$  contour divides the AR cross-  
 325 section diagonally at 50% of AR length (Fig. 3c). Recall that the geopotential height field  
 326 tilts westward with height in an extratropical cyclone, required by the hydrostatic bal-  
 327 ance in a baroclinic wave (Holton & Hakim, 2013). This implies that towards the head  
 328 of the AR ( $> 50\%$  length), the upper troposphere above the AR is governed by posi-  
 329 tive pressure anomalies (not shown).

330 The pressure, temperature and wind distributions are in accordance with a clas-  
 331 sical frontal system associated with an extratropical cyclone (e.g. Petterssen (1936); Keyser  
 332 et al. (1988); Hoskins and Bretherton (1972)). Scale analysis suggests that in the semi-  
 333 geostrophic theory, the horizontal momentum equation in the frontal system can be ap-  
 334 proximated by geostrophic balance in the along-front direction ( $u = u_g$ ), but the ageostrophic  
 335 component becomes non-negligible in the cross-front direction ( $v = v_g + v_a$ ) (K. Brown-  
 336 ington, 1985; Holton & Hakim, 2013). The existence of ageostrophic winds implies verti-  
 337 cal motions, which are shown in Fig. 4, in cross sections at 25, 50 and 75% of the AR  
 338 length from the equatorward end.

339 It can be seen that vertical motion gets increasingly stronger from the tail to the  
 340 head of the AR (Fig. 4). This is consistent with the relationship between ARs and WCBs,  
 341 the latter of which have been characterised by both vertical and horizontal motions, in  
 342 contrast to ARs that are identified solely from horizontal fields (K. Browning, 1985; Cordeira  
 343 et al., 2013; Ralph et al., 2020). For instance, according to the WCB definition by Wernli

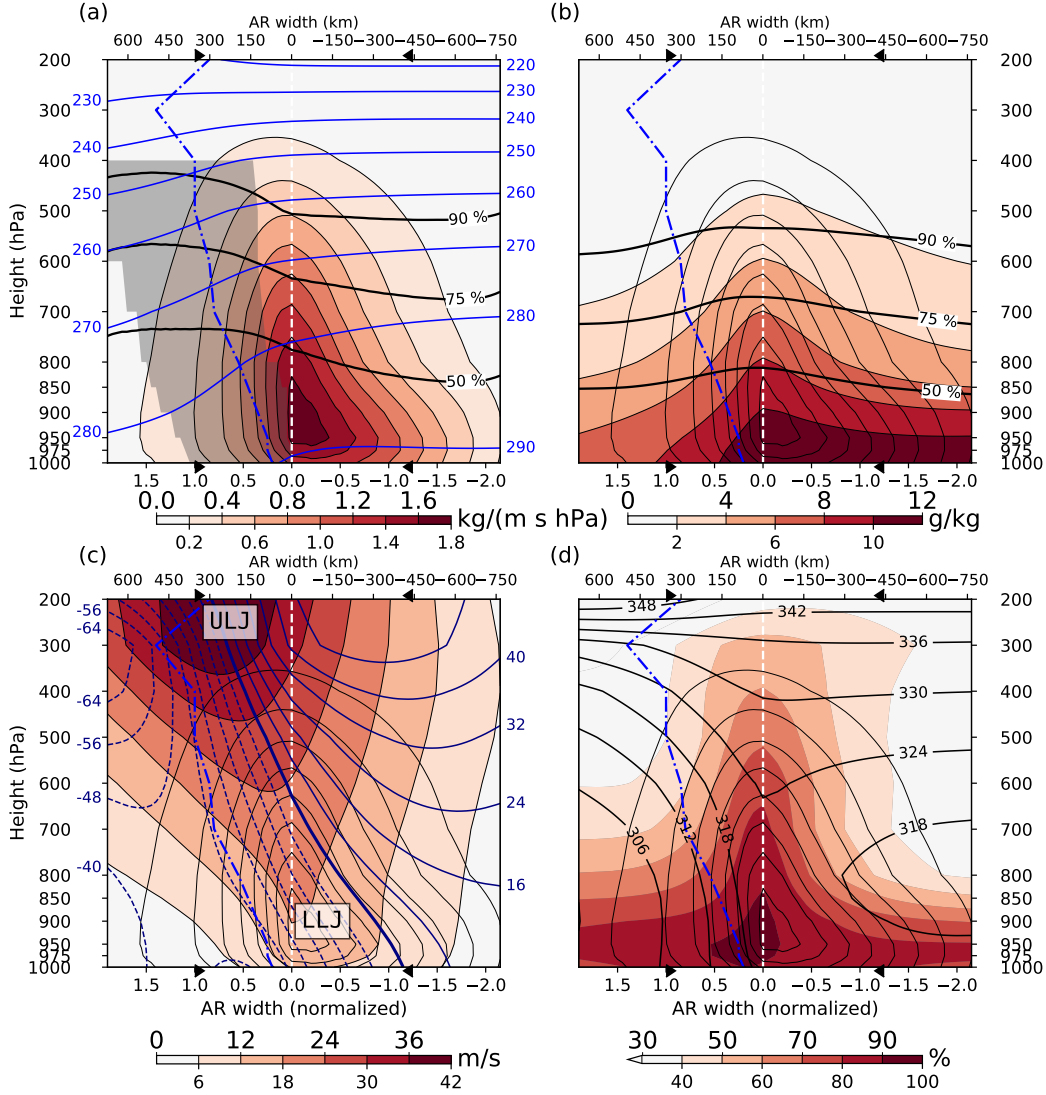


**Figure 3.** Composite cross-sections of North Pacific ARs. (a) shows the along-axis moisture flux (as color shading, in  $kg/(m\ s\ hPa)$ ), and temperature (as blue contour lines, with an interval of  $10\ K$ ). Thick black contours show the height at which 50, 75 and 90 % of the total IVT are reached, integrating from the ground up. Grey shading represents regions with strong baroclinicity (horizontal temperature gradient  $\leq -1K/100\ km$ ), and the dash-dotted curve denotes the maximum (negative) temperature gradient at each level and represents the position of the cold front. The same IVT contours are also shown in (b), (c) and (d) as thin black contours, and the same front line is recreated in subsequent subplots. The x-axis is the width of the AR, normalized to the average AR width of  $800\ km$ . Black triangles at the top/bottom x-axes denote the lateral boundaries of the AR, with the cold (warm) side located on the left (right) hand side. (b) IWV profile as color shading, in  $g/kg$ . Thick black contours show the height at which 50, 75 and 90 % of the total IWV are reached, integrating from the ground up. (c) along-axis horizontal wind speed as color shading, in  $m/s$ . Thick blue contours show the geopotential height anomalies, with an interval of  $8\ m$ . Negative anomalies are plotted as dashed contours. Locations of the upper-level-jet (ULJ) and low-level-jet (LLJ) are labeled. (d) relative humidity profile as color shading, in %. Thick black contours show the equivalent potential temperature, in  $K$ .

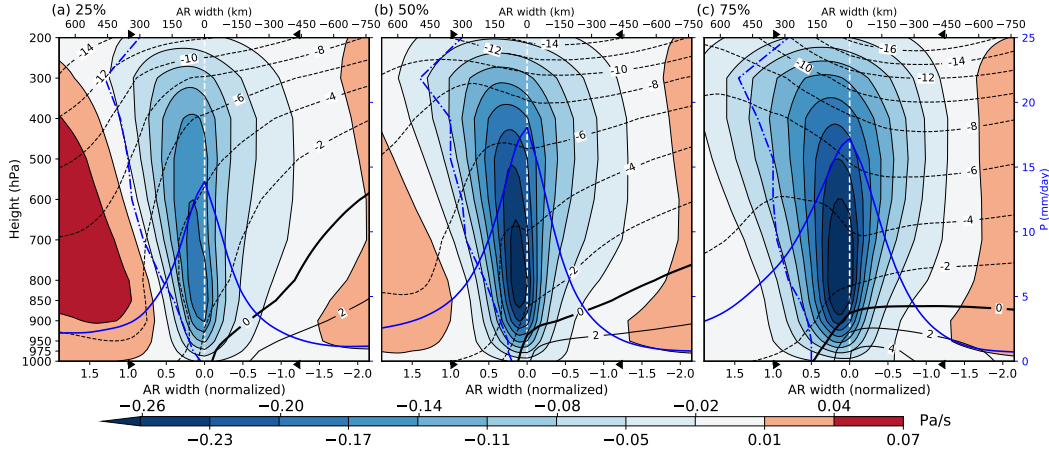


**Figure 4.** Composite cross-sections at 25 (a), 50 (b) and 75% (c) of the AR length. Color shading shows the pressure velocity (in  $Pa/s$ ). Black contours show the cross-axis horizontal wind speeds, with an interval of  $2\ m/s$ . Positive cross-axis wind is directed to the left. Solid blue curves show the precipitation distribution (in  $mm/day$ ), plotted onto the y-axis on the right. In each subplot, the dash-dotted curve shows locations of minimum negative temperature gradient at each level. The x-axis is width of the AR, normalized to the average width of  $800\ km$ . Black triangles at the top/bottom x- axes denote the lateral boundaries of the AR, with the cold (warm) side located on the left (right) hand side.

344 and Davies (1997), a WCB is defined as the region with ascending motions stronger than  
 345  $600\ hPa$  per  $48h$ . By this criterion, the WCB is only observed at the end of the AR, be-  
 346 yond the 75% length (not shown).

347 Accompanied with the concentrated ascending motion is the precipitation distri-  
 348 bution that centers at the AR axis but with a flatter tail on the cold side (Fig. 4). This  
 349 may be explained by the higher relative humidity levels on this side (Fig. 3d), and is also  
 350 consistent with the so-called “anafront” model that a cold front tends to have upslid-  
 351 ing warm air overriding the surface cold front, creating post-frontal precipitation (K. A. Brown-  
 352 ing & Monk, 1982; K. Browning, 1985; K. A. Browning & Roberts, 1996). The higher  
 353 rain rates on the cold side is also consistent with a satellite-based composite created from  
 354 46 Eastern Pacific ARs (Ralph et al., 2004). Descending motion is found on both flanks  
 355 of the AR, particularly towards the tail of the AR where the cold front is strongest, form-  
 356 ing the cross-frontal secondary circulation with the pre-frontal ascending motions.

357 Most previous studies focused on the along-axis fluxes/winds in an AR’s cross-sections,  
 358 and few has examined the vertical structure of the cross-axis components. Note that the  
 359 cross-axis horizontal winds are dominated by winds from the cold side (Fig. 4). Cross-  
 360 axis warm winds are only found in the bottom section of the troposphere, with decreas-  
 361 ing thickness from the tail to the head of the AR. The transition from positive (warm  
 362 advection) to negative (cold advection) with height is the manifestation of the veering  
 363 wind, as a result of the thermal wind relationship associated with the warm front. Simi-  
 364 larly, across the cold front at the tail half of the AR (Fig. 4a, b), the isotaches have near  
 365 vertical profiles within  $1000\text{--}500\ hPa$ . Combined with the vertically increasing along-  
 366 front winds (Fig. 3c), this indicates an anti-clockwise rotation of the cross-frontal winds  
 367 with height, and is the thermal wind relationship manifest as backing winds. Both of the  
 368 veering and backing winds help rotate the moisture fluxes from their respective sides to  
 369 align with the AR axis, thus forming a mechanism that collects moisture from the lat-

370 eral boundaries of the AR. However, it is worth noting that thermal winds as derived  
 371 from geostrophic balance do not create any horizontal divergence, unless the Coriolis pa-  
 372 rameter is not treated as a constant (Benedetto, 1957; Alpert et al., 1995). At frontal  
 373 scale of a few hundred kilometers, the change of Coriolis parameter is negligible, there-  
 374 fore the strong vertical motion at the AR center can not be explained by the backing and  
 375 veering winds.

376 As predicated by the semi-geostrophic theory, ageostrophic winds in the cross-front  
 377 direction have comparable importance as the geostrophic component. Their relative roles  
 378 in the AR horizontal moisture fluxes are examined further in the next section.

### 379 3.3 Moisture fluxes due to geostrophic and ageostrophic winds

380 Layered geostrophic and ageostrophic winds and moisture fluxes are first computed  
 381 before fed into the straightening algorithm, and cross-sectional profiles averaged across  
 382 the AR length are shown in Fig. 5. Along-axis winds and moisture fluxes are both dom-  
 383 inated by the geostrophic component (Fig. 5a,b). Ageostrophic winds show a local min-  
 384 imum at the upper level jet level, extending downward along the front line, pointing in  
 385 the opposite direction of the geostrophic counterpart (Fig. 5c). This is due to the rear-  
 386 ward pointing pressure gradient force created by the westward tilting low pressure center  
 387 as explained previously. Combined with the low humidity level above the mid-troposphere  
 388 (Fig. 3b), this offsetting ageostrophic component makes little difference to the along-axis  
 389 moisture fluxes.

390 Cross-axis geostrophic winds contribute most of the moisture fluxes into the AR  
 391 region from the cold side (Fig. 5d, e), while ageostrophic winds, created by the leftward  
 392 pointing pressure gradient force and surface friction, are responsible for the moisture in-  
 393 puts from the warm side within a more vertically confined region (Fig. 5d, f). These two  
 394 branches converge towards the AR center, providing the water vapor contents for the along-  
 395 axis moisture fluxes. Also note that the ageostrophic winds have a local maximum ahead  
 396 of the surface front, and another in the upper troposphere along the upper level front  
 397 (Fig. 5f). These two maxima help strengthening the temperature gradients at the lower  
 398 and upper jet locations, and tilting the frontal zone backwards. Dynamically, they also  
 399 serve as a forcing term for the along-axis geostrophic wind, according to the momentum  
 400 equation in the semi-geostrophic framework (Holton & Hakim, 2013):  $\frac{Du_g}{Dt} = fv_a$ , where  
 401  $u_g$  is the along-axis geostrophic wind,  $v_a$  the cross-axis ageostrophic wind, and  $f$  the Cori-  
 402 olis parameter. On the other hand, geostrophic winds contribute a much greater amount  
 403 of moisture from the cold side (Fig. 5e, see also analyses in later section). The lower hu-  
 404 midity level on the cold side is over compensated by a much stronger cross-frontal geostrophic  
 405 wind. Furthermore, cold geostrophic advection in the mid-troposphere and warm ageostrophic  
 406 advection in the boundary layer help reduce static stability, creating a zone of neutral  
 407 moist static stability at the core of the AR (Fig. 3d), consistent with sounding obser-  
 408 vations (Ralph et al., 2005; Neiman et al., 2013). Diabatic processes fostered by the near  
 409 saturated and ascending air are likely to contribute significantly as well. In summary,  
 410 both geostrophic and ageostrophic winds make indispensable thermodynamic and dy-  
 411 namic contributions to the high moisture fluxes of ARs. Consequently, their evolution-  
 412 ary changes are likely to get reflected in the changes of the AR moisture fluxes as well.  
 413 This subject is explored in the next section.

### 414 3.4 Evolutionary changes of AR moisture fluxes

415 The same AR entity is first tracked through space and time using the method in-  
 416 troduced in Xu et al. (2020b). Only tracks lasting for at least 24 hours are retained. Daily  
 417 composites from genesis (0H) up to day-5 (120H), which is roughly the 80% percentile  
 418 in the duration distribution (see Fig. S10), are shown in Fig. 6. All composites are the

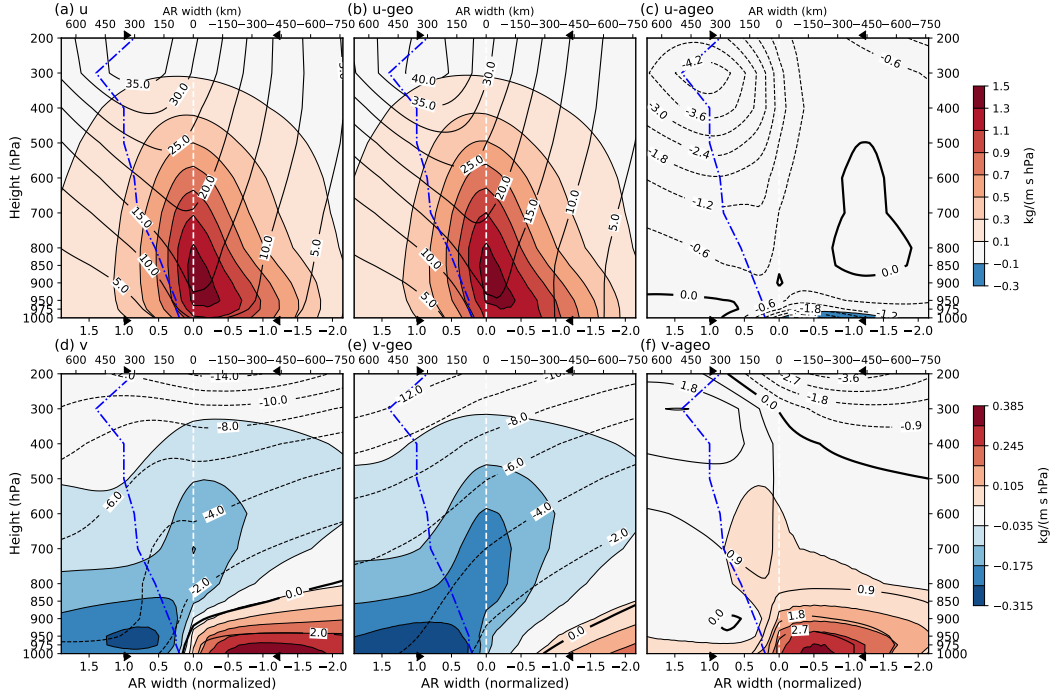


**Figure 5.** Composites of geostrophic and ageostrophic components of the along-axis (top row) and cross-axis (bottom row) moisture fluxes and winds. (a) the along-axis moisture flux (color shading, in  $kg/(m\ s\ hPa)$ ) and along-axis wind speeds (black contours, in  $m/s$ ), and their respective geostrophic components in (b) and ageostrophic components in (c). (d) the cross-axis moisture flux (color shading, in  $kg/(m\ s\ hPa)$ ) and cross-axis wind (black contour, in  $m/s$ ), and their respective geographic component in (e) and ageostrophic components in (f). All results are the average across the entire AR length.

419 averages across the entire AR length. Considering their dominant role, only the mois-  
 420 ture fluxes by geostrophic winds are shown for the along-axis direction.

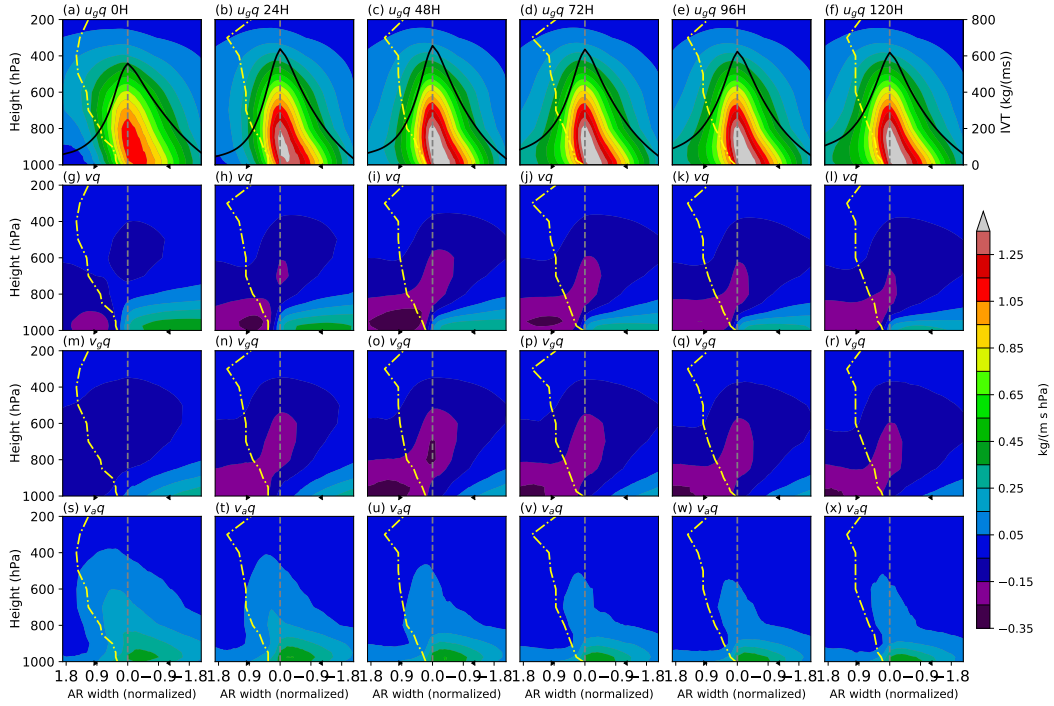


**Figure 6.** Composite cross-sectional geostrophic and ageostrophic moisture fluxes (color shading, in  $kg/(m s hPa)$ ). From left to right, columns are 0, 24, 48, 72, 96 and 120H after the first detection of the AR track. Top row shows the along-axis geostrophic moisture flux. Solid black curve is the IVT profile (in  $Kg/(m s)$ ), plotted onto the y-axis on the right hand side. Second row shows the total cross-axis fluxes, which are decomposed into the geostrophic component in the third row, and the ageostrophic component in the last row. In all subplots, the yellow dash-dot curve denotes the location of the cold front, and black triangles at the bottom edge denote the lateral boundary the AR. All profiles are averaged across the entire AR length.

421 It can be seen that ARs tend to reach their peak IVT intensity about two days after  
 422 genesis (top row in Fig. 6), followed by a gradual decline afterwards. This is in phase  
 423 with the variation of cold side moisture fluxes (2nd row in Fig. 6), which are mostly con-  
 424 tributed by the geostrophic component (3rd row in Fig. 6). Moisture fluxes from the warm  
 425 side, on the other hand, show a gradual retreat from the genesis time (2nd row in Fig. 6).  
 426 This is a result of weakening geostrophic (3rd row in Fig. 6) and ageostrophic (4th row  
 427 in Fig. 6) fluxes from the warm side. However, the local maximum of ageostrophic fluxes  
 428 in front of the surface cold front persists throughout the process. The above evolution-  
 429 ary changes are further validated by time series of the moisture fluxes given in Fig. 7a.  
 430 Vertical integral of the along-axis geostrophic flux ( $\langle u_g q \rangle$ ) reaches its peak value about  
 431 48 hours after genesis, in sync with the variation of cold side cross-axis geostrophic flux  
 432 ( $-\langle v_g q \rangle_c$ ). Warm side cross-axis ageostrophic flux ( $\langle v_a q \rangle_w$ ) makes a bigger con-  
 433 tribution during first 24 hours, serving as the dominant factor for lateral moisture in-  
 434 puts during genesis, but gets surpassed by the cold side counterpart and continues to weaken  
 435 afterwards.

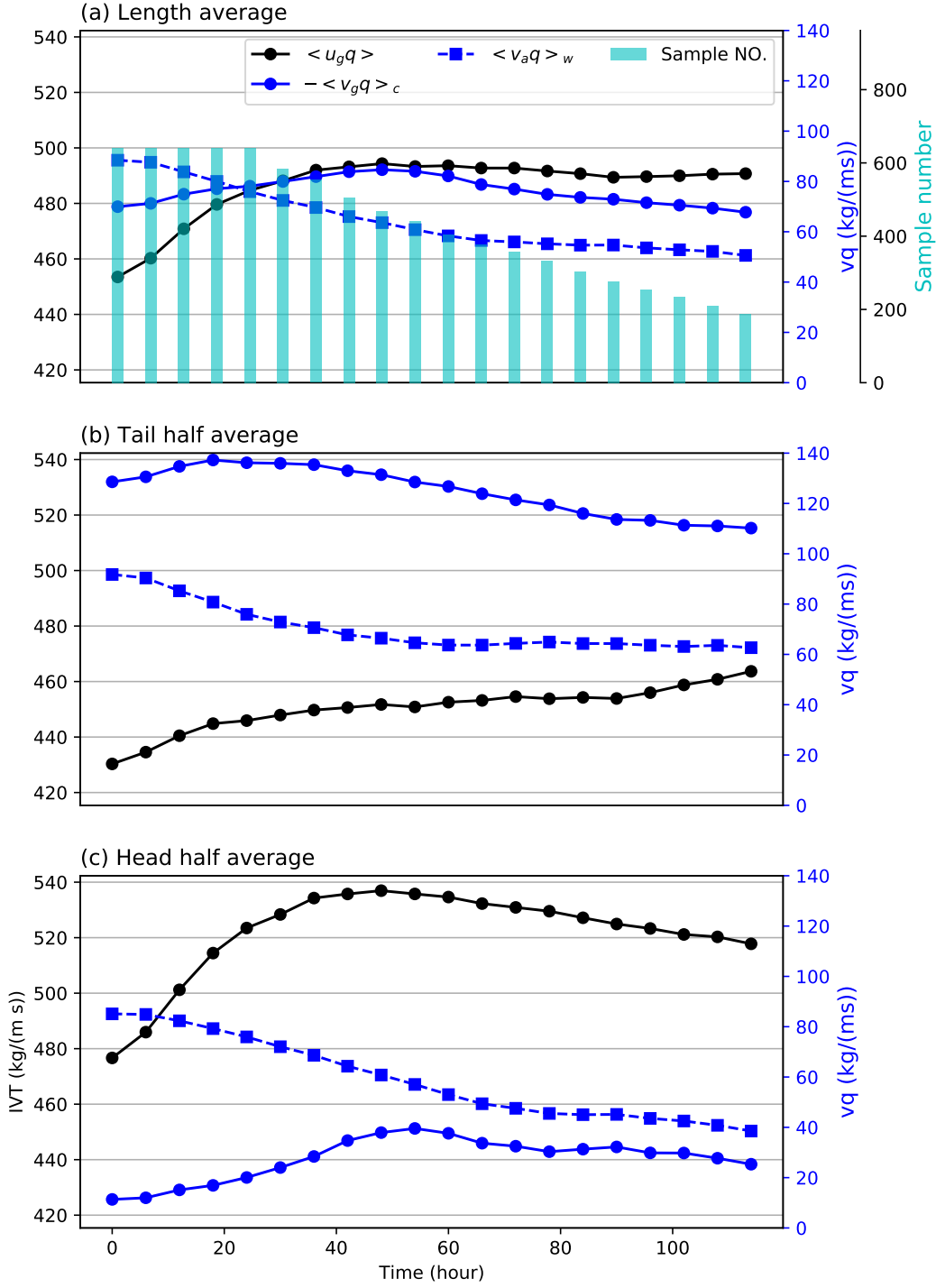


**Figure 7.** Time series of vertical integrals of moisture fluxes (in  $kg/(ms)$ ) following the evolution of ARs. Black curve shows the along-axis moisture flux by geostrophic winds ( $\langle u_g q \rangle$ ), solid blue curve shows the negative of cross-axis geostrophic moisture flux from the cold side ( $-\langle v_g q \rangle_c$ ), and dashed curve the cross-axis ageostrophic moisture flux from the warm side ( $\langle v_a q \rangle_w$ ). The two blue curves are plotted onto the y-axis on the right hand side. (a) shows the averages across the entire AR length, (b) the averages of the tail half (0 – 50% length) of the ARs, and (c) the averages of the head half (50 – 100% length). The number of AR samples in each 6-hourly time step are shown as cyan bars in (a), plotted onto the 2nd y-axis on the right.

436 Note that longer-lasting ARs get progressively rarer, as shown in Fig. 7a, and the  
 437 above evolutionary analyses do not distinguish ARs with possibly different life spans. To  
 438 investigate these effects, we further split the AR tracks into a short duration group where  
 439 ARs last for 24–72 hours, and a long duration group where ARs last for longer than  
 440 72 hours. The chosen 72 hour threshold is slightly above the median of the duration dis-  
 441 tribution (see Fig. S10). Time series of moisture fluxes in these two groups are given in  
 442 Fig. S11 in the Supplementary. It can be seen that ARs with short and long durations  
 443 share similar evolutionary changes during the first 48 hours that are consistent with the  
 444 above analyses (with the exception that ageostrophic moisture fluxes from the warm side  
 445 get surpassed by the cold side geostrophic component even sooner in the short duration  
 446 group).

447 After the peak intensity time, moisture fluxes from both sides weaken with the along-  
 448 axis fluxes, suggesting a possible relationship between the lateral moisture inputs and  
 449 the intensity of the AR IVT. However, IVT can also be affected by changes in the along-  
 450 axis winds. To further distinguish the dynamical and thermodynamical contributions,  
 451 changes in the along-axis geostrophic moisture fluxes at different stages are decomposed  
 452 into a dynamical component ( $q\Delta u_g$ ), a thermodynamical component ( $u_g\Delta q$ ), and a co-  
 453 variance term ( $\Delta(u_gq)$ ), where  $\Delta$  denotes a time difference from 0H. The results are given  
 454 in Fig. 8. Compared with 0H, along-axis geostrophic moisture fluxes get stronger within  
 455 a narrow band along the AR axis, and within a layer below 800 *hPa* level behind the front  
 456 (Fig. 8a-e). This is a combined effect from the dynamical component as the primary in-  
 457 tensification mechanism ( $q\Delta u_g$ , 2nd row in Fig. 8), and the thermodynamical compo-  
 458 nent as a partially offsetting mechanism ( $u_g\Delta q$ , 3rd row in Fig. 8).

459 The changes in the along-axis geostrophic winds (Fig. 8f-j) are largely consistent  
 460 with the changes in cross-frontal pressure gradients ( $\frac{g}{f}\Delta(\frac{\partial Z}{\partial x})$ ) (Fig. 8a-e). When mul-  
 461 tiplied with a vertically decreasing humidity distribution, the resultant changes in geostrophic  
 462 moisture fluxes are confined to the mid-lower troposphere. On the other hand, moisture  
 463 level drops at both sides of the AR, and to a lesser extent, along the AR axis (Fig. 8k-  
 464 o). Largest humidity decrease is found below  $\sim 700$  *hPa* behind the front, consistent  
 465 with Dacre et al. (2015). When multiplied with the strong jet wind speeds, this decrease  
 466 largely offsets the dynamical intensification effects ahead of the front in the mid-troposphere.  
 467 The greater extents of humidity decreases at the lateral boundaries compared with the  
 468 core region also reflect the convergence of moisture into the AR interior, and the over-  
 469 all decrease of humidity a net export of water vapor within the AR region. Lastly, con-  
 470 tribution made by the covariance term ( $\Delta u_g\Delta q$ , Fig. 8p-t) is much weaker, but tend to  
 471 offset the along-axis moisture fluxes on the cold side.

472 A similar decomposition is performed on the cross-axis moisture fluxes, but sep-  
 473 arately for geostrophic and ageostrophic components. Only the significant terms are shown  
 474 in Fig. S12 in the Supplementary. The results, combined with the above along-axis coun-  
 475 terparts, suggest that the evolutionary changes of cold and warm side moisture fluxes  
 476 as shown in Fig. 6 are mostly due to the dynamical terms of the geo- and ageostrophic  
 477 winds, with some offsetting effects from the thermodynamical terms.

478 To summarize the evolutionary changes: ARs tend to experience an early IVT in-  
 479 tensification period during the first two days after genesis, dynamically powered by the  
 480 intensifying along-axis geostrophic winds. Strong moisture fluxes from the warm sector  
 481 and the rapidly strengthening fluxes from the cold side help provide extra moisture, how-  
 482 ever, they are not enough to offset the dropping level of moisture within the AR domain.  
 483 Consequently, although the along-axis geostrophic winds remain as strong in later stages  
 484 of AR development, reduced moisture level becomes an increasingly important factor.  
 485 Meanwhile, moisture supplies from the cold (warm) side also drop, largely due to the weak-  
 486 ening cross-frontal geostrophic (ageostrophic) winds. In essence, water vapor content be-  
 487 comes a limiting factor for further IVT intensification.

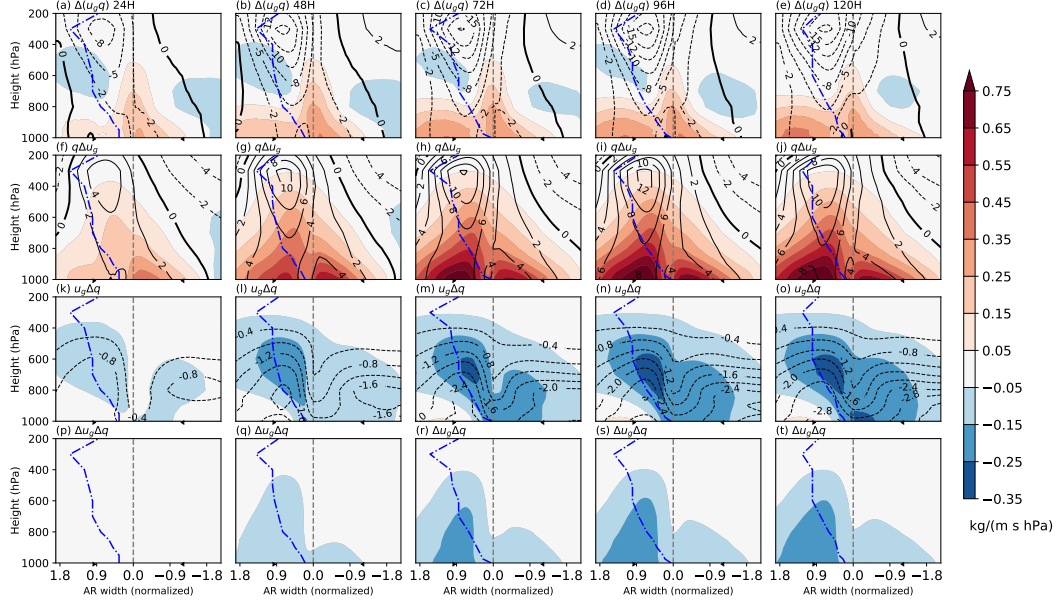


**Figure 8.** Changes in the along-axis moisture fluxes during AR evolution. Columns are the differences between 24, 48, 72, 96 and 120H from 0H. First row shows the differences of geostrophic moisture fluxes ( $\Delta(u_g q)$ ) as color shading, in  $kg/(m s hPa)$ . Black contours show the changes in the cross-axis pressure gradient, scaled by a constant factor of  $g/f_0 = 10/10^{-4} m/s$  to a unit of  $m/s$ . Second row shows the changes contributed by the dynamical term ( $q\Delta u_g$ ) as color shading, in  $kg/(m s hPa)$ . Black contours show the changes in the along-axis geostrophic winds, in  $m/s$ . Third row shows the changes contributed by the thermodynamical term ( $u_g \Delta q$ ) as color, with the changes in humidity itself drawn as black contours, in  $g/kg$ . The last row shows the contribution made by the covariance term ( $\Delta u_g \Delta q$ ). In all subplots, the blue dash-dot curve denotes the location of the cold front, and black triangles at the bottom edge denote the lateral boundary the AR. All profiles are averaged across the entire AR length.

488 The above analyses also reveal that during the majority of AR life cycle, moisture  
 489 fluxes within the AR region are directed from the cold side. This is also observed in the  
 490 plane-view IVT composite in Fig. 2a and the cross-sections in Fig. 5. However, the lat-  
 491 eral flux distribution is not axially symmetric along the axis. This is illustrated by the  
 492 time series in Fig. 7b,c that, a greater amount of moisture fluxes are directed into the  
 493 AR domain from the cold side in the tail half of the AR, and the opposite is observed  
 494 in the head half, but with a smaller difference between the two sides. Therefore, the lat-  
 495 eral moisture influx averaged across the course of the AR is dominated by that from the  
 496 cold side, and complex patterns of moisture fluxes exist within the AR domain.

497 Furthermore, Dacre et al. (2019) previously proposed a “feeder airstream” mech-  
 498 anism and suggested that fluxes from the warm sector are the primary moisture source  
 499 for the intensification of ARs. This discrepancy may be caused by the different reference  
 500 systems used in the analyses: a cyclone-relative frame of reference in their study, and  
 501 an Earth-relative frame of reference in this work so far. The next section gives a closer  
 502 look at the spatial patterns of AR moisture transports and compare them in these two  
 503 frames of reference.

### 504 3.5 AR Moisture transports in Earth- and AR-relative frames of ref- 505 erence

506 The typical moisture transports pattern by an AR in an *Earth-relative* frame of  
 507 reference is represented by the cross-boundary moisture fluxes across the bounding box  
 508 of the straightened AR, averaged across the entire evolution stage (Fig. 9). Moisture fluxes  
 509 across the air-sea interface are approximated by vertical fluxes at the 1000 *hPa* level, and  
 510 the top “lid” has been omitted for its low humidity level. Moisture fluxes across the four  
 511 vertical sides, i.e. the cold side (Fc), warm side (Fw), rear side (Fw) and frontal side (Ff)  
 512 are displayed as an unfolded box (see Fig. 9b for a schematic). Positive fluxes are de-  
 513 fined as outward and vice versa. Side-integrated moisture fluxes are computed using an  
 514 average AR width of 800 *km* and an average length of 3500 *km*. The total precipitation  
 515 within the bounding box is also integrated and scaled to a unit of  $10^8 \text{kg/s}$ , as an extra  
 516 moisture output term.

517 It can be seen that the frontal and rear sides have similar patterns of cross-boundary  
 518 fluxes (Fig. 9e, c), but with stronger magnitude in the former ( $2.5$  versus  $-2.1 \times 10^8 \text{kg/s}$ ,  
 519 Fig. 9g). This is consistent with the head-tail half differences shown in Fig. 7b,c, and im-  
 520 plies a “tunneling-out” effect of moisture along the course of the AR. The largest mois-  
 521 ture input term is the geostrophic fluxes from the cold side, with a stronger magnitude  
 522 than that from the rear side, although the moisture flux intensities are much weaker. Ageostrophic  
 523 fluxes pointing towards the cold side account for a small offset. The relationship is re-  
 524 versed on the warm side: geostrophic winds create a  $\sim 1.0 \times 10^8 \text{kg/s}$  moisture output,  
 525 which is overcompensated by a slightly stronger ageostrophic moisture input, reflecting  
 526 the same head-tail distinction mentioned above. Vertical fluxes from the bottom is much  
 527 smaller compared with other four sides, and precipitation serves as the largest output  
 528 term with a magnitude of  $\sim 2.7 \times 10^8 \text{kg/s}$ . Overall, the atmosphere is slightly dried  
 529 out at a rate of  $\sim 0.2 \times 10^8 \text{kg/s}$  due to the existence of the AR.

530 Note that the vertical side integration involves the multiplication of horizontal mois-  
 531 ture flux with area. The straightening algorithm does a satisfactory job in preserving  
 532 scalar and vector fields, however, shape distortion is inevitable, and might affect the areal  
 533 integration. To help validate the results and evaluate the possible effects from shape dis-  
 534 tortion, the cross-boundary flux analysis is repeated on a subset of ARs whose starting  
 535 and ending points fall into specific regions. For the central North Pacific sector, the start-  
 536 ing box is chosen to be  $20 - 35^\circ \text{N}$ ,  $150 - 165^\circ \text{E}$ , and the ending box  $40 - 55^\circ \text{N}$ ,  $170 -$   
 537  $185^\circ \text{E}$ . The samples are further filtered by the length and average axis curvature (see  
 538 Appendix for definition) both being within one standard deviation around their respec-

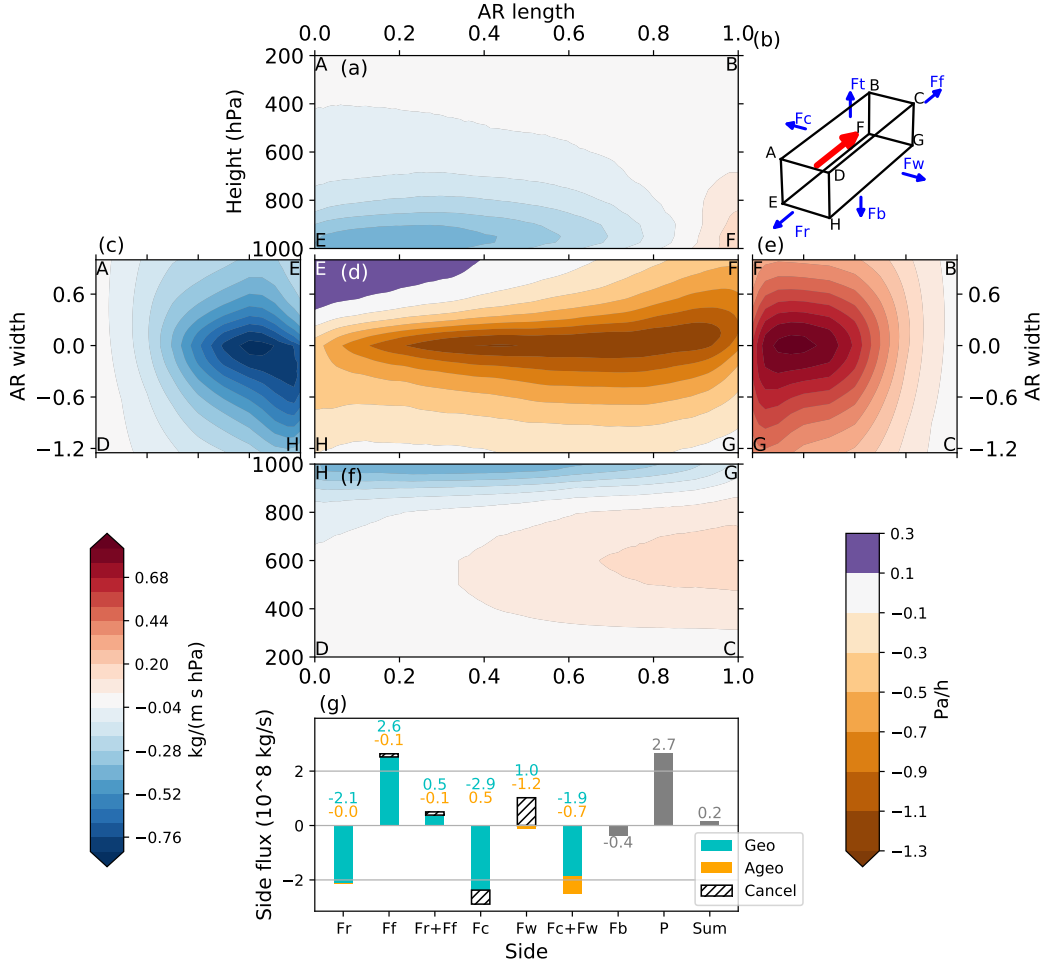


**Figure 9.** Moisture fluxes across the bounding box of a typical North Pacific AR. A 3D schematic showing the bounding box is given in (b), and the red arrow shows the mean IVT direction. The moisture fluxes across the cold side ( $F_c$ ) is given in (a), the rear side ( $F_r$ ) in (c), bottom side ( $F_b$ ) in (d), frontal side ( $F_f$ ) in (e), and the warm side ( $F_w$ ) in (f). Vertices of the bounding box are labeled at the corner of each side, for instance, the side  $ABFE$  is the one facing the cold front, whose contour is given in (a). Note that the four vertical sides share the colorbar at the bottom-left corner, in units of  $\text{kg}/(\text{m s hPa})$ , and the bottom side uses a separate colorbar at the bottom right, in units of  $\text{Pa}/\text{h}$ . Positive contours denote outward moisture fluxes, and vice versa. (g) shows the side-integrated outward moisture fluxes across the five sides, in  $10^8 \text{ kg/s}$ . Fluxes due to geostrophic winds are plotted in cyan, and those by ageostrophic winds in orange. If the ageostrophic component has an opposite sign as the geostrophic counterpart, the geostrophic part that gets offset is shown as hatched. Also shown are the sum of the rear and frontal sides ( $F_r + F_f$ ), the sum of the cold and warm sides ( $F_c + F_w$ ), the areal-integrated precipitation ( $P$ , in  $10^8 \text{ kg/s}$ ), and the sum of all five sides plus precipitation.

539 tive means. These requirements should guarantee a reasonable shape and location co-  
 540 herence of the AR samples in the composite. The results are given in Fig. S13 in the Sup-  
 541 plementary. Another composite in the western North Pacific (Fig. S14), and one in the  
 542 eastern North Pacific are also created (Fig. S15). In all sector-specific results, the re-  
 543 lative importance of fluxes from different directions is consistent with the composite tak-  
 544 ing into all North Pacific ARs: moisture export by precipitation is much stronger than  
 545 the input by evaporation, consistent with Cordeira et al. (2013). The most important  
 546 moisture input comes from the cold side geostrophic fluxes, concentrated on the tail half  
 547 of the AR. Large cancellation is observed between inward and outward moisture fluxes  
 548 on the warm side. And the sum of the frontal and rear side fluxes creates a small net  
 549 moisture deficit, indicating the “tunneling out” effect of the AR.

550 However, the lateral moisture fluxes are expected to be different when changing from  
 551 an Earth-relative to AR-relative frame of reference. To illustrate this, the translation ve-  
 552 locity ( $\mathbf{V}_t$ ) of an AR is first quantified using a centered difference scheme on the 6-hourly  
 553 AR locations, which are approximated by the IVT-weighted centroids. Then “effective  
 554 winds” (Sohn & Park, 2010; Zahn & Allan, 2011) of  $\mathbf{IVT}$  are computed as:  $\mathbf{V}_e \equiv \mathbf{IVT}/IWV$ .  
 555 The AR-relative effective winds are defined as  $\mathbf{V}_r \equiv \mathbf{V}_e - \mathbf{V}_t$ , and AR-relative  $\mathbf{IVT}$   
 556 as  $\mathbf{V}_r \cdot IWV$ . A composite is created using ARs whose starting point falls within the  
 557 box of  $20 - 35^\circ N, 135 - 150^\circ E$ , and end point in the box of  $40 - 55^\circ N, 155 - 170^\circ E$ .  
 558 The results are shown in Fig. 10.

559 It can be seen that the effective winds within ARs are largely in geostrophic bal-  
 560 ance and follow the  $Z850'$  contours (Fig. 10a). When multiplied with  $IWV$ , this creates  
 561 the shuttle-like IVT distribution in the straightened view (Fig. 10b). The average AR  
 562 translation velocity is northeastward, more or less the same as the propagation speed of  
 563 the extratropical cyclone (Fig. 10c). However, in the AR-relative frame of reference, ef-  
 564 fective winds change into easterlies (Fig. 10e), indicating a faster AR movement speed  
 565 than the low level winds, consistent with Dacre et al. (2019). These easterly AR-relative  
 566 horizontal winds bring in moisture from the warm side of the cyclone, and diverge at the  
 567 eastern boundary of the AR into two branches (Fig. 10e, f). One branch steers north-  
 568 ward wrapping around the low pressure center, and the other branch southwestward to-  
 569 wards the tail of the AR. This northward branch enters the WCB, and the diverging east-  
 570 erly flow is the “feeder-airstream” proposed by Dacre et al. (2019).

571 Moisture fluxes associated with the translational and relative velocities also con-  
 572 tribute differently to the total AR IVT. Fig. 10 shows that the translational winds con-  
 573 tribute most of the total IVT in the tail half of the AR, across the rear and cold sides.  
 574 Based on the previous analyses, this corresponds to the largely geostrophic moisture ad-  
 575 vections that are carried along by the moving AR-cyclone couple. The northward branch  
 576 of the “feeder-airstream”, on the other hand, makes bigger contributions within the head  
 577 half of the AR, representing the newly collected moisture by the fast moving AR.

578 It is worth noting a few precautions when making a direct comparison with the AR  
 579 formation mechanism proposed by Dacre et al. (2019). Firstly, the  $1500\text{ km}$  radius in their  
 580 cyclone-centric composites does not cover the full extent of the trailing AR. Secondly,  
 581 the similarity between the cyclone movement speed, AR movement speed and low-level  
 582 wind speed makes the cyclone- or AR- relative wind estimates very sensitive to their dif-  
 583 ferences. Lastly, the time period examined by Dacre et al. (2019) is centered around the  
 584 maximum cyclone intensity and is likely to emphasize more on the early development  
 585 stage of ARs, while no time period preference is enforced in the composite in Fig. 10.  
 586 Despite these precautions, the broad structure of the AR-relative moisture transports  
 587 is in accordance with the argument that the “feeder-airstream” is an important mois-  
 588 ture source for the AR-cyclone couple: the northward branch of “feeder-airstream” forms  
 589 the head half of the AR, and the rearward branch advects warm, moist air from the warm  
 590 sector towards the AR, thus preconditioning the atmosphere with vapor contents that  
 591 would soon be collected by the propagating AR. The warm side contribution is also found

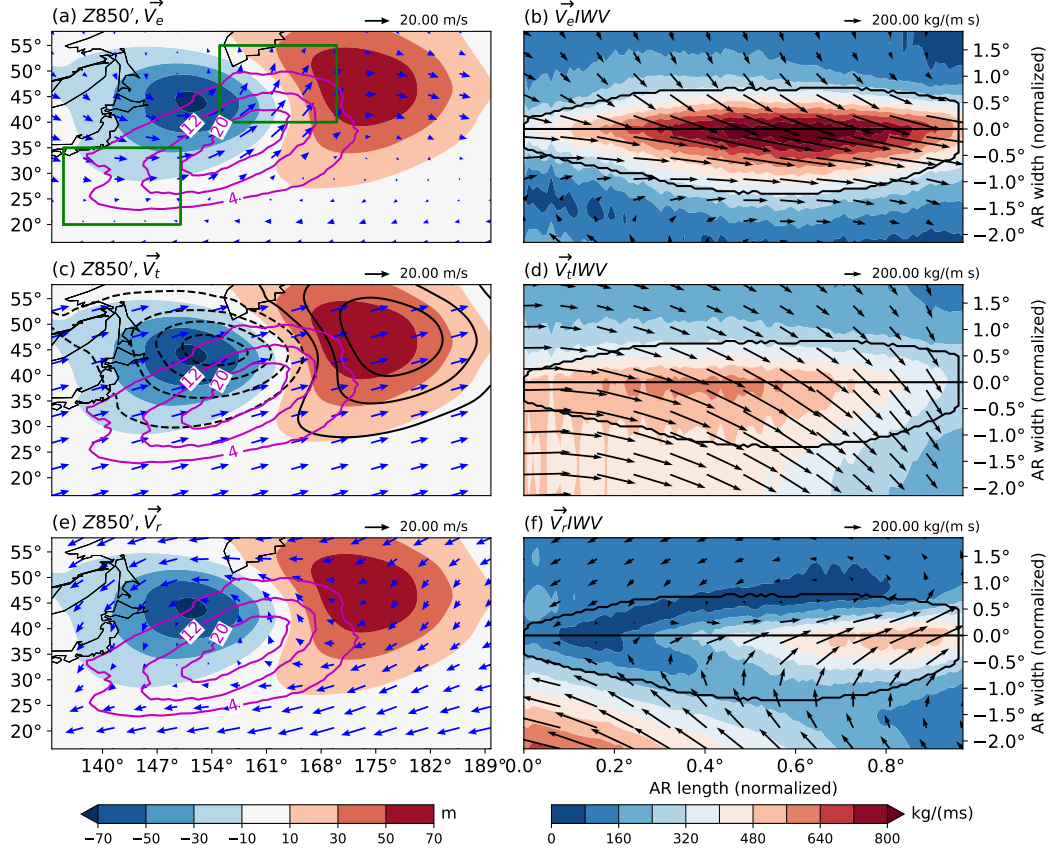


**Figure 10.** Left column shows the composite of 850  $hPa$  geopotential height anomalies ( $Z_{850'}$ ) as color shading (in  $m$ ), and AR occurrences as pink contours (in number of ARs per year). The composite is created by selecting ARs whose starting point falls within the box of  $20 - 35^{\circ}N, 135 - 150^{\circ}E$ , and end point the box of  $40 - 55^{\circ}N, 155 - 170^{\circ}E$ . The two boxes are plotted as green rectangles in (a). Black contours in (c) show the  $Z_{850'}$  distribution 6-hours later, to indicate the movement of the cyclone. Blue vectors show the effective winds  $\mathbf{V}_e$  in (a), the mean translation velocity  $\mathbf{V}_t$  of the ARs in (c), and the AR-relative effective winds  $\mathbf{V}_r$  in (e). Right column shows the straightened IVT of the selected ARs as color shading (in  $kg/(m s)$ ). (b) shows the effective winds as black arrows and the IVT attributed to that  $\vec{V}_e I WV$ . (d) and (f) show the corresponding components due to the mean translation velocity  $\vec{V}_t I WV$  and AR-relative effective winds  $\vec{V}_r I WV$ , respectively.

592 to be strongest during the first 24 hours after genesis (will only be stronger once trans-  
 593 formed into the AR-relative frame of reference), and is therefore consistent with the peak  
 594 cyclone intensity timing adopted by Dacre et al. (2019). Additionally, analyses in this  
 595 work also highlight the importance of the geostrophic moisture advection in the tail half  
 596 of the AR. This component captures a large portion of the overall AR moisture trans-  
 597 port during the majority of AR life cycle, and represents the moisture transport carried  
 598 along the propagating AR-cyclone couple.

#### 599 4 Conclusions and discussions

600 In this work, we developed a method to straighten the scalar and vector fields as-  
 601 sociated with an AR into a composite-ready form, thus making the otherwise cumber-  
 602 some AR composite analyses from gridded atmospheric data more practically achievable.  
 603 By applying the straightening methods on different vertical levels on a large sample size,  
 604 a three dimensional composite of a typical North Pacific AR is reconstructed. The re-  
 605 sults depict a typical AR-cyclone relationship consistent with previous findings: a North  
 606 Pacific AR is typically found within the southeastern quadrant of an extratropical cy-  
 607 clone, aligning along and in front of the surface cold front.

608 The straightening method allows for a more accurate depiction of an AR's cross-  
 609 sections, many aspects of which can be verified by sounding- and satellite-based obser-  
 610 vations. Both the IVT and IWV profiles display an asymmetrical distribution about the  
 611 AR axis. A backward tilting frontal zone is observed, and a low level jet is found ahead  
 612 of the surface front, within of core of the AR. The AR core also collocates with a zone  
 613 of high relative humidity, neutral moist static stability and concentrated vertical motions.

614 ARs have an important dynamical feature that they stride across two major length  
 615 scales: synoptic scale in the along-axis direction where geostrophic balance dominates,  
 616 and meso-scale in the cross-axis direction where ageostrophic processes are of equal im-  
 617 portance (K. Browning, 1985; Holton & Hakim, 2013; Cordeira et al., 2013). At meso-  
 618 scale, a thermally direct cross-sectional secondary circulation is observed, with strong  
 619 ascendings in front of the surface cold front and descendings behind it, consistent with  
 620 the semi-geostrophic theory. Boundary layer ageostrophic winds help converge moisture  
 621 from the warm sector, and also help maintain the strong temperature gradients across  
 622 the front. As a result, the thermal wind balance tends to be interrupted, and along-front  
 623 winds intensified by the Coriolis force as a restoring mechanism, contributing to the strong  
 624 AR IVT. These highlight the close relationship between AR development and fronto-  
 625 genesis processes.

626 During the first two days of AR life cycle, the moisture influx from the lateral bound-  
 627 aries, together with the strengthening along-axis geostrophic winds, lead to the peak IVT  
 628 intensities during the life time of the AR. After about 48 hours since genesis, the lat-  
 629 eral moisture influx weakens, and the AR IVT intensity starts to decline as well. Dynamical-  
 630 thermodynamical analyses indicate that although the along-axis winds remain as strong,  
 631 moisture level within the AR region drops and becomes a limiting factor for further IVT  
 632 intensification. The lower humidity levels at higher latitudes, into which most ARs prop-  
 633 agate, may also contribute. On the other hand, the atmosphere is dried out by the re-  
 634 siding AR, reflecting AR's role as an effective poleward moisture transport mechanism  
 635 (Zhu & Newell, 1998).

636 From an Earth-relative perspective, fluxes from the cold side form the primary mois-  
 637 ture source for the atmosphere resided by an AR, replenishing the net moisture loss along  
 638 the course of the AR. This is also the primary vapor source that offsets the deleterious  
 639 effect from precipitation, consistent with Cordeira et al. (2013). Moisture advection from  
 640 the warm side is mostly attributed to ageostrophic winds confined within the boundary  
 641 layer. The backing and veering winds associated with their respective fronts help rotate

642 the uplifted moisture fluxes to align with the AR axis, thus forming a moisture aggre-  
 643 gation mechanism that gathers moisture from the lateral boundaries. Recall that the AR  
 644 is aligned along the cold front, and the cold side cross-frontal moisture fluxes are mostly  
 645 geostrophic. Therefore, the cold side moisture input is fundamentally created by the baro-  
 646 clinicity of the system in that the angle formed by the isotherms and isobars give rise to  
 647 the cold side moisture influx.

648 The AR-relative moisture transport pattern is consistent with the “feeder-airstream”  
 649 concept proposed by Dacre et al. (2019). This downstream easterly flow diverges into  
 650 two branches, with the northward branch entering the head of the AR. The southward  
 651 branch does not directly form the body of the AR, but preconditions the immediate down-  
 652 stream atmosphere with more vapor contents. The component that bridges the Earth-  
 653 and AR-relative moisture transports is the moisture fluxes by translational winds. In the  
 654 tail half of the AR, total AR IVT is mostly contributed by translational moisture fluxes,  
 655 representing the largely geostrophic moisture advections carried along by the propagat-  
 656 ing AR/cyclone couple. In the head half of the AR, total AR IVT is mostly contributed  
 657 by the northward branch of the AR-relative “feeder-airstream”, suggesting that the east-  
 658 ward propagating AR-cyclone couple is “claiming” more moist-loaded atmospheric ter-  
 659 ritory, “harvesting” more vapor contents along the way. Note that it does not necessar-  
 660 ily mean that the water vapor has been staying still in the downstream atmosphere, wait-  
 661 ing to be collected. They may have gone through a long tropical or mid-latitude trajec-  
 662 tory before coming into the AR (Bao et al., 2006).

663 The divergent movement of the AR-relative “feeder-airstream” and the swift di-  
 664 rectional transition within the course of an AR are related to the similarity between the  
 665 AR-cyclone movement speed and the speed of low level winds. This sensitive response  
 666 to AR-cyclone movement speed may have some important morphological implications  
 667 on ARs. For instance, the diverging flows stretches the AR along its axis, and may serve  
 668 as an AR length growth mechanism. This stretching effect works on the AR continuously,  
 669 and may explain the delayed timing of peak length compared to peak IVT intensity as  
 670 observed in Xu et al. (2020a). It is also observed that the maximum precipitation center  
 671 within the AR composite tends to shift rearward as the AR propagates from west-  
 672 ern into central North Pacific (not shown). This may not be an evolution-related fea-  
 673 ture, because ARs originating from central Pacific have their precipitation center already  
 674 shifted. Instead, we speculate that this is due to the longitudinal differences in the cy-  
 675 clone movement speed. Cyclones (and therefore their accompanying ARs) tend to travel  
 676 faster within the mid-latitude jet streams (Hoskins & Hodges, 2002)). Based on the pat-  
 677 tern in Fig. 10, the AR-relative moisture fluxes become more northeasterly with a faster  
 678 translation speed, creating a longer northward branch of the “feeder-airstream” and a  
 679 longer WCB. However, further analyses are required to validate this hypothesis.

680 Lastly, this work has a number of limitations. The AR composites take in all AR  
 681 samples without any discriminations on seasons, latitudes, lengths, orientations and shapes  
 682 etc.. Therefore, the results only reflect the general structure of a North Pacific AR, with  
 683 considerable case-to-case differences masked out. Moreover, the AR-cyclone model is also  
 684 highly simplified and generalized, and the true picture in particular cases may be con-  
 685 siderably more complex. For instance, it is common for an extratropical cyclone to have  
 686 more than one cold fronts (e.g. Ralph et al. (2004)), and it is also possible for an AR  
 687 to be associated with two cyclones (Sodemann & Stohl, 2013; Dacre et al., 2019), or none  
 688 at all (Z. Zhang et al., 2019). ARs can also deviate away from the cyclonic curvature as  
 689 depicted in the typical AR-cyclone composite, and have straight, or anti-cyclonic shapes,  
 690 possibly affected by the interactions with the jet streams (Cordeira et al., 2013), or dif-  
 691 ferent types of Rossby wave breaking (Ralph et al., 2020). The meso-scale frontal struc-  
 692 ture also comes with various configurations (K. A. Browning & Monk, 1982; K. Brown-  
 693 ing, 1985; K. A. Browning & Roberts, 1996; Schultz et al., 1998). We did not quanti-  
 694 tatively examine the frontogenesis processes and the interactions with ARs, nor the adi-

695 abatic processes associated with the pre-frontal ascendings, which may play a crucial role  
696 in the maintenance of ARs. Due to shape distortions involved in the straightening pro-  
697 cess, the bounding box moisture flux analysis should only be regarded as a qualitative  
698 estimate of the relative importance of moisture fluxes from different directions, and a quan-  
699 titative water vapor budget analysis is not warranted in this configuration.

## 700 **Acknowledgments**

701 This research is funded by the National Natural Science Foundation of China No.  
702 41930970 and No. 41776013. This research is partially supported by the International  
703 Laboratory for High-Resolution Earth System Prediction (IHESP). Dataset (ERA-INTERIM  
704 reanalysis) used in this work is publicly available to registered users at [https://www.ecmwf](https://www.ecmwf.int/en/forecasts/datasets/reanalysis-datasets/era-interim)  
705 [.int/en/forecasts/datasets/reanalysis-datasets/era-interim](https://www.ecmwf.int/en/forecasts/datasets/reanalysis-datasets/era-interim)

## 5 Appendix

### 5.1 Constructing the resample matrix for straightening interpolation

Perpendicular profiles are sampled along the AR axis to form the “resample matrix”. Each perpendicular profile consists of one point on the AR axis (black dots in Fig. 1b), plus 14 evenly spaced points on the warm side of the AR covering a distance of  $10^\circ$  ( $\sim 1112 \text{ km}$ , shown as red dots in Fig. 1b), and 21 evenly spaced points on the cold side, covering a distance of  $15^\circ$  ( $\sim 1668 \text{ km}$ , blue dots in Fig. 1b). This gives a profile of  $N = 35$  sample points with an even spacing of  $0.71^\circ$ , roughly the same as the native  $0.75^\circ$  resolution of the input ERA-I data. The asymmetry between the warm and cold sides is because an AR typically appears around an extratropical cyclone and a longer limb on the cold side helps capture the low pressure center of the cyclone.

Putting these oriented profiles into a regular array gives the resample matrix  $R$ , with a dimension of  $N \times M$ , where  $N = 35$  is the number of points along each profile, and  $M$  the number of profiles. Unlike  $N$  that has a fixed value, the value of  $M$  varies as the AR length, therefore, it is further normalized (using bi-linear interpolation) to a fixed length of  $M = 100$ , making the straightened image composite-ready. The target grid to interpolate onto has the same shape as  $R$  but with x-coordinates being the AR length and the y-coordinates the AR width, both measured in  $\text{km}$ .

The direction of the profile is determined by finding a unit vector ( $\boldsymbol{\theta}_i$ ) at each interior axis point ( $P_i$ ) that evenly divide the angle formed by two consecutive line segments ( $\overline{P_i, P_{i-1}}$  and  $\overline{P_i, P_{i+1}}$ ). Formally, let  $P_i = (x_i, y_i, z_i)$  and  $P_{i+1} = (x_{i+1}, y_{i+1}, z_{i+1})$  being two consecutive points on the AR axis, and  $O$  being the origin of the unit sphere on which the Cartesian coordinates  $x, y, z$  are defined. Then the vector  $\mathbf{T}_{i,i+1}$  tangent at  $P_i$  in the plane formed by  $\overline{OP_i}$  and  $\overline{OP_{i+1}}$  can be found by:

$$\mathbf{T}_{i,i+1} = (\mathbf{P}_i \times \mathbf{P}_{i+1}) \times \mathbf{P}_i = \mathbf{P}_{i+1} - \mathbf{P}_i(\mathbf{P}_i \cdot \mathbf{P}_{i+1}) \quad (1)$$

where  $\times$  is cross product. Another tangent  $\mathbf{T}_{i,i-1}$  can be similarly found. Using this definition,  $\boldsymbol{\theta}_i$  can be defined as the average of the two unit tangents at  $P_i$

$$\boldsymbol{\theta}_i = \frac{1}{2} \left( \frac{\mathbf{T}_{i,i+1}}{\|\mathbf{T}_{i,i+1}\|} + \frac{\mathbf{T}_{i,i-1}}{\|\mathbf{T}_{i,i-1}\|} \right) \quad (2)$$

An exception to this that is when the two consecutive segments form a straight line,  $\boldsymbol{\theta}_i$  will be a zero vector. In such cases  $\boldsymbol{\theta}_i$  is chosen to be  $\boldsymbol{\theta}_{\text{warm}}$  defined next.

The direction of the warm side is determined by the vector of the axis segment  $\overline{P_i, P_{i+1}}$  rotated *clockwise* by 90 degrees:

$$\boldsymbol{\theta}_{\text{warm}} = -\hat{\mathbf{k}} \times \overline{P_i, P_{i+1}} \quad (3)$$

where  $\hat{\mathbf{k}}$  is the unit vector of the vertical dimension. Recall that the AR axis is directed by definition, so will be the  $\overline{P_i, P_{i+1}}$  vector. Then the sign of  $\boldsymbol{\theta}_i$  is reversed (if needed) so that it always aligns with  $\boldsymbol{\theta}_{\text{warm}}$  (in that their dot product being positive) and points towards the warm side. Note that this is effectively the opposite process to the thermal wind derivation where the direction of the horizontal temperature gradient is rotated *anti-clockwise* by 90 degrees to give the thermal wind direction. The cold side is simply the opposite to the warm side:  $\boldsymbol{\theta}_{\text{cold}} \equiv -\boldsymbol{\theta}_{\text{warm}}$ .

The angle of the profile line with respect to the North is defined as  $\arccos(-\boldsymbol{\theta}_{\text{cold}} \cdot \mathbf{T}_{i,N})$ , where  $\mathbf{T}_{i,N}$  is the local tangent vector pointing towards the North.

745 **5.2 Determining the average curvature of an AR's axis**

746 The average axis curvature is defined as the angles formed by consecutive line seg-  
 747 ment pairs ( $\alpha_i = \arccos(\overline{\mathbf{P}_i, \mathbf{P}_{i-1}} \cdot \overline{\mathbf{P}_i, \mathbf{P}_{i+1}})$ ) along the AR axis, summed over the axis  
 748 ( $\sum_i \alpha_i$ ). The cyclonic direction is defined as positive curvature and vice versa.

749 **References**

- 750 Alpert, P., Shay-El, Y., & Heifetz, E. (1995). A comment on the geostrophic wind  
 751 divergence. *Quarterly Journal of the Royal Meteorological Society*, *121*, 227-  
 752 228. doi: 10.1002/qj.49712152111
- 753 Arora, T., Dhir, R., & Mahajan, M. (2017). An algorithm to straighten the bent hu-  
 754 man chromosomes. In *2017 fourth international conference on image informa-  
 755 tion processing (iciip)* (p. 1-6). doi: 10.1109/ICIIP.2017.8313772
- 756 Bao, J.-W., Michelson, S. A., Neiman, P. J., Ralph, F. M., & Wilczak, J. M. (2006).  
 757 Interpretation of enhanced integrated water vapor bands associated with ex-  
 758 tratropical cyclones: Their formation and connection to tropical moisture.  
 759 *Monthly Weather Review*, *134*, 1063-1080. doi: 10.1175/mwr3123.1
- 760 Benedetto, F. (1957). Analysis of the vorticity and divergence of the thermal wind  
 761 in pure geostrophic flow. *Archiv für Meteorologie, Geophysik und Bioklimatolo-  
 762 gie Serie A*, *10*, 20-28. doi: 10.1007/bf02247826
- 763 Browning, K. (1985). Conceptual models of precipitation systems. *Meteor. Mag.*,  
 764 *114*, 293-319.
- 765 Browning, K. A., & Monk, G. A. (1982). A simple model for the synoptic analysis  
 766 of cold fronts. *Quarterly Journal of the Royal Meteorological Society*, *108*, 435-  
 767 452. doi: https://doi.org/10.1002/qj.49710845609
- 768 Browning, K. A., & Pardoe, C. W. (1973). Structure of low-level jet streams ahead  
 769 of mid-latitude cold fronts. *Quarterly Journal of the Royal Meteorological Soci-  
 770 ety*, *99*, 619-638. doi: https://doi.org/10.1002/qj.49709942204
- 771 Browning, K. A., & Roberts, N. M. (1996). Variation of frontal and precipitation  
 772 structure along a cold front. *Quarterly Journal of the Royal Meteorological So-  
 773 ciety*, *122*, 1845-1872. doi: 10.1002/qj.49712253606
- 774 Cordeira, J. M., Ralph, F. M., & Moore, B. J. (2013). The development and evo-  
 775 lution of two atmospheric rivers in proximity to western north pacific tropical  
 776 cyclones in october 2010. *Monthly Weather Review*, *141*, 4234-4255. doi:  
 777 10.1175/mwr-d-13-00019.1
- 778 Dacre, H. F., Clark, P. A., Martínez-Alvarado, O., Stringer, M. A., & Lavers, D. A.  
 779 (2015). How do atmospheric rivers form? *Bulletin of the American Meteorolog-  
 780 ical Society*, *96*, 1243-1255. doi: 10.1175/BAMS-D-14-00031.1
- 781 Dacre, H. F., Martínez-Alvarado, O., & Mbengue, C. O. (2019). Linking atmo-  
 782 spheric rivers and warm conveyor belt airflows. *Journal of Hydrometeorology*,  
 783 *20*, 1183-1196. doi: 10.1175/jhm-d-18-0175.1
- 784 Dee, D. P., Uppala, S. M., Simmons, A. J., Berrisford, P., Poli, P., Kobayashi, S., ...  
 785 Vitart, F. (2011). The era-interim reanalysis: configuration and performance  
 786 of the data assimilation system. *Quarterly Journal of the Royal Meteorological  
 787 Society*, *137*, 553-597. doi: 10.1002/qj.828
- 788 Eiras-Barca, J., Ramos, A. M., Pinto, J. G., Trigo, R. M., Liberato, M. L. R., &  
 789 Miguez-Macho, G. (2018). The concurrence of atmospheric rivers and ex-  
 790 plosive cyclogenesis in the north atlantic and north pacific basins. *Earth  
 791 System Dynamics*, *9*, 91-102. Retrieved from [http://dx.doi.org/10.5194/  
 792 esd-9-91-2018](http://dx.doi.org/10.5194/esd-9-91-2018) doi: 10.5194/esd-9-91-2018
- 793 Frenger, I., Gruber, N., Knutti, R., & Münnich, M. (2013). Imprint of southern  
 794 ocean eddies on winds, clouds and rainfall. *Nature Geoscience*, *6*, 608-612. doi:  
 795 10.1038/ngeo1863
- 796 Gimeno, L., Nieto, R., Vázquez, M., & Lavers, D. A. (2014). Atmospheric rivers: a

- 797 mini-review. *Frontiers in Earth Science*, 2. doi: 10.3389/feart.2014.00002
- 798 Held, I. M., & Soden, B. J. (2006). Robust responses of the hydrological cycle to  
799 global warming. *Journal of Climate*, 19, 5686-5699. doi: 10.1175/JCLI3990.1
- 800 Holton, J. R., & Hakim, G. J. (2013). Chapter 9 - mesoscale circulations. In  
801 J. R. Holton & G. J. Hakim (Eds.), *An introduction to dynamic meteorology*  
802 *(fifth edition)* (Fifth Edition ed., p. 279 - 323). Boston: Academic Press. doi:  
803 <https://doi.org/10.1016/B978-0-12-384866-6.00009-X>
- 804 Hoskins, B. J., & Bretherton, F. P. (1972). Atmospheric frontogenesis models:  
805 Mathematical formulation and solution. *Journal of the Atmospheric Sciences*,  
806 29, 11-37. doi: 10.1175/1520-0469(1972)029<0011:afmmfa>2.0.co;2
- 807 Hoskins, B. J., & Hodges, K. I. (2002). New perspectives on the northern hemi-  
808 sphere winter storm tracks. *Journal of the Atmospheric Sciences*, 59, 1041-  
809 1061. doi: 10.1175/1520-0469(2002)059<1041:NPOTNH>2.0.CO;2
- 810 Jahani, S., & Kamaledin Setarehdan, S. (2012). Centromere and length detection  
811 in artificially straightened highly curved human chromosomes. *International*  
812 *Journal of Biological Engineering*, 2, 56-61. doi: 10.5923/j.ijbe.20120205.04
- 813 Jourdain, N. C., Barnier, B., Ferry, N., Vialard, J., Menkes, C. E., Lengaigne, M.,  
814 & Parent, L. (2014). Tropical cyclones in two atmospheric (re)analyses and  
815 their response in two oceanic reanalyses. *Ocean Modelling*, 73, 108-122. doi:  
816 10.1016/j.ocemod.2013.10.007
- 817 Keyser, D., Reeder, M. J., & Reed, R. J. (1988). A generalization of petterssen's  
818 frontogenesis function and its relation to the forcing of vertical motion.  
819 *Monthly Weather Review*, 116, 762-781. doi: 10.1175/1520-0493(1988)  
820 116<0762:agopff>2.0.co;2
- 821 Knaff, J. A., Longmore, S. P., & Molenar, D. A. (2014). An objective satellite-based  
822 tropical cyclone size climatology. *Journal of Climate*, 27, 455-476. doi: 10  
823 .1175/JCLI-D-13-00096.1
- 824 Knippertz, P., Wernli, H., & Gläser, G. (2013). A global climatology of tropical  
825 moisture exports. *Journal of Climate*, 26, 3031-3045. doi: 10.1175/jcli-d-12  
826 -00401.1
- 827 Liu, X., Ma, X., Chang, P., Jia, Y., Fu, D., Xu, G., ... Patricola, C. M. (2021).  
828 Ocean fronts and eddies force atmospheric rivers and heavy precipita-  
829 tion in western north america. *Nature Communications*, 12. Retrieved  
830 from <http://dx.doi.org/10.1038/s41467-021-21504-w> doi: 10.1038/  
831 s41467-021-21504-w
- 832 Mundhenk, B. D., Barnes, E. A., & Maloney, E. D. (2016). All-season climatology  
833 and variability of atmospheric river frequencies over the north pacific. *Journal*  
834 *of Climate*, 29(13), 4885-4903. doi: 10.1175/JCLI-D-15-0655.1
- 835 Neiman, P. J., Ralph, F. M., Moore, B. J., Hughes, M., Mahoney, K. M., Cordeira,  
836 J. M., & Dettinger, M. D. (2013). The landfall and inland penetration of a  
837 flood-producing atmospheric river in arizona. part i: Observed synoptic-scale,  
838 orographic, and hydrometeorological characteristics. *Journal of Hydrometeorol-*  
839 *ogy*, 14, 460-484. doi: 10.1175/jhm-d-12-0101.1
- 840 Newell, R. E., & Zhu, Y. (1994). Tropospheric rivers: A one-year record and a pos-  
841 sible application to ice core data. *Geophysical Research Letters*, 21, 113-116.  
842 doi: 10.1029/93gl03113
- 843 Petterssen, S. (1936). Contribution to the theory of frontogenesis. *Geofys. Publ.*, 11,  
844 1-27.
- 845 Ralph, F. M., Dettinger, M. D., Cairns, M. M., Galarneau, T. J., & Eylander, J.  
846 (2018). Defining "atmospheric river": How the glossary of meteorology helped  
847 resolve a debate. *Bulletin of the American Meteorological Society*, 99, 837-839.  
848 doi: 10.1175/bams-d-17-0157.1
- 849 Ralph, F. M., Dettinger, M. D., Rutz, J., Jonathan, & Waliser, D. E. (2020). *Atmo-*  
850 *spheric rivers*. Gewerbestrasse 11, 6330 Cham, Switzerland: Springer Interna-  
851 tional Publishing. doi: 10.1007/978-3-030-28906-5

- 852 Ralph, F. M., Iacobellis, S. F., Neiman, P. J., Cordeira, J. M., Spackman, J. R.,  
853 Waliser, D. E., . . . Fairall, C. (2017). Dropsonde observations of total inte-  
854 grated water vapor transport within north pacific atmospheric rivers. *Journal*  
855 *of Hydrometeorology*, *18*, 2577-2596. doi: 10.1175/JHM-D-17-0036.1
- 856 Ralph, F. M., Neiman, P. J., & Rotunno, R. (2005). Dropsonde observations in low-  
857 level jets over the northeastern pacific ocean from caljet-1998 and pacjet-2001:  
858 Mean vertical-profile and atmospheric-river characteristics. *Monthly Weather*  
859 *Review*, *133*, 889-910. doi: 10.1175/mwr2896.1
- 860 Ralph, F. M., Neiman, P. J., & Wick, G. A. (2004). Satellite and caljet aircraft  
861 observations of atmospheric rivers over the eastern north pacific ocean dur-  
862 ing the winter of 1997/98. *Monthly Weather Review*, *132*, 1721-1745. doi:  
863 10.1175/1520-0493(2004)132<1721:SACAOO>2.0.CO;2
- 864 Schultz, D. M., Keyser, D., & Bosart, L. F. (1998). The effect of large-scale flow  
865 on low-level frontal structure and evolution in midlatitude cyclones. *Monthly*  
866 *Weather Review*, *126*, 1767-1791. doi: 10.1175/1520-0493(1998)126<1767:  
867 teolsf>2.0.co;2
- 868 Sodemann, H., & Stohl, A. (2013). Moisture origin and meridional transport in  
869 atmospheric rivers and their association with multiple cyclones\*. *Monthly*  
870 *Weather Review*, *141*, 2850-2868. doi: 10.1175/mwr-d-12-00256.1
- 871 Sohn, B. J., & Park, S. C. (2010). Strengthened tropical circulations in past three  
872 decades inferred from water vapor transport. *Journal of Geophysical Research*  
873 *Atmospheres*, *115*, D15112. doi: 10.1029/2009JD013713
- 874 Wernli, B. H., & Davies, H. C. (1997). A lagrangian-based analysis of extratropical  
875 cyclones. i: The method and some applications. *Quarterly Journal of the Royal*  
876 *Meteorological Society*, *123*, 467-489. doi: 10.1002/qj.49712353811
- 877 Wick, G. A., Neiman, P. J., & Ralph, F. M. (2013). Description and validation  
878 of an automated objective technique for identification and characteriza-  
879 tion of the integrated water vapor signature of atmospheric rivers. *IEEE*  
880 *Transactions on Geoscience and Remote Sensing*, *51*(4), 2166-2176. doi:  
881 10.1109/TGRS.2012.2211024
- 882 Xu, G., Ma, X., Chang, P., & Wang, L. (2020a). A comparison of northern hemi-  
883 sphere atmospheric rivers detected by a new image-processing based method  
884 and magnitude-thresholding based methods. *Atmosphere*, *11*, 628. doi:  
885 10.3390/atmos11060628
- 886 Xu, G., Ma, X., Chang, P., & Wang, L. (2020b). Image-processing-based atmo-  
887 spheric river tracking method version 1 (ipart-1). *Geoscientific Model Develop-*  
888 *ment*, *13*, 4639-4662. doi: 10.5194/gmd-13-4639-2020
- 889 Zahn, M., & Allan, R. P. (2011). Changes in water vapor transports of the ascend-  
890 ing branch of the tropical circulation. *Journal of Geophysical Research*, *116*,  
891 D18111. doi: 10.1029/2011JD016206
- 892 Zhang, X., Ma, X., & Wu, L. (2019). Effect of mesoscale oceanic eddies on extra-  
893 tropical cyclogenesis: A tracking approach. *Journal of Geophysical Research:*  
894 *Atmospheres*, *124*, 6411-6422. doi: 10.1029/2019jd030595
- 895 Zhang, Z., Ralph, F. M., & Zheng, M. (2019). The relationship between extratrop-  
896 ical cyclone strength and atmospheric river intensity and position. *Geophysical*  
897 *Research Letters*, *46*, 1814-1823. doi: 10.1029/2018gl079071
- 898 Zhou, Y., Kim, H., & Guan, B. (2018). Life cycle of atmospheric rivers: Identifica-  
899 tion and climatological characteristics. *Journal of Geophysical Research: Atmo-*  
900 *spheres*, *123*. doi: 10.1029/2018jd029180
- 901 Zhu, Y., & Newell, R. E. (1994). Atmospheric rivers and bombs. *Geophysical Re-*  
902 *search Letters*, *21*, 1999-2002. Retrieved from [http://dx.doi.org/10.1029/](http://dx.doi.org/10.1029/94gl01710)  
903 [94gl01710](http://dx.doi.org/10.1029/94gl01710) doi: 10.1029/94gl01710
- 904 Zhu, Y., & Newell, R. E. (1998). A proposed algorithm for moisture fluxes from at-  
905 mospheric rivers. *Monthly Weather Review*, *126*, 725-735. doi: 10.1175/1520  
906 -0493(1998)126<0725:APAFMF>2.0.CO;2